

Modeling present and future ~~bedrock~~ rock wall permafrost distribution in the Sisimiut mountain area, West Greenland

Marco Marcer^{1,2}, Pierre-Allain Duvillard^{3,4}, Soňa Tomaškovičová¹, Steffen Ringsø Nielsen^{2,5}, André Revil⁴, and Thomas Ingeman-Nielsen¹

¹DTU Sustain, Bygning RSTorvet, Bygning 115, 2800 Kgs. Lyngby, Denmark

²Arctic DTU, Siimuup Aqquataa 32, B-1280, 3911 Sisimiut, Greenland

³NAGA Geophysics, 12 Allée du lac de Garde, Le Bourget du lac, France

⁴EDYTEM, Université Savoie Mont-Blanc, CNRS (UMR 5204), 73370 Le Bourget du Lac, France

⁵KTI Råstofskolen - Greenland School of Minerals and Petroleum, Adammp Aqq. 2, 3911 Sisimiut, Greenland

Correspondence: Marco Marcer (marcma@byg.dtu.dk)

Abstract. ~~Bedrock~~ Rock wall permafrost is a feature of cold mountain ranges that was found responsible for the increase of rock fall and landslide activity in several regions across the globe. In Greenland, ~~bedrock~~ rock wall permafrost has received so far little attention from the scientific community, despite mountains are a predominant feature on the ice-free coastline and landslide activity is significant. With this study, we aim to move a first step towards the characterization of ~~bedrock~~ rock wall permafrost in Greenland. Our study area covers 100 km² of mountain terrain around the town of Sisimiut – 68° N on the West Coast. We first acquire ground surface temperature data for ~~the hydrological year across the period 2020 /21– 2022~~ to model bedrock surface temperatures time series from weather forcing on the period 1850 - 2022. ~~Using a topographical downscaling method based on digital elevation model, we then create climatic boundary conditions for 1D and 2D heat transfer numerical simulations at the landscape level~~ We then create weather forcing heat transfer transient simulations. In this way we obtain permafrost distribution maps and ad-hoc simulations for complex topographies. Our ~~results are validated by comparison with model results are compared to~~ temperature data from two lowland boreholes (100 m depth) and geophysical data describing frozen/unfrozen conditions across a mid-elevation mountain ridge. Finally, we use regional carbon pathway scenarios 2.6 and 8.5 to evaluate future evolution of ground temperatures until the end of the 21st century. Our ~~results indicate a sporadic permafrost distribution~~ data and simulation describe discontinuous permafrost distribution in rock walls up to roughly 400 m.a.s.l., ~~while future~~ Future scenarios suggest a decline of deep frozen bodies up to 800 m.a.s.l., i.e. the highest summits in the area. In summary, this study depicts a picture of warm permafrost in this area, highlighting its sensitivity to ongoing climate change.

1 Introduction

~~The term "permafrost" defines ground presenting temperatures that remain below 0 °C for at least two consecutive years.~~ In cold mountain regions, complex topography influences shading, snow distribution and ground type, causing a highly variable distribution of ground temperatures and permafrost in steep rock walls (Etzelmüller, 2013). Several field studies describe a

significant correlation between warming climate, ~~mountain-rock wall~~ permafrost degradation and increased slope instability, observed as rockfall frequency (Ravel and Deline, 2011; Gallach et al., 2020), ~~and~~ large rockslide occurrence (Patton et al., 2019; Guerin et al., 2020; Frauenfelder et al., 2018; Walter et al., 2020), ~~high elevation infrastructure destabilization (?) and debris permafrost creep rate increase (?)~~. Therefore, understanding the spatial distribution of ~~mountain-rock wall~~ permafrost and its future evolution is a key step in ~~understanding these hazards~~ defining potential hazard areas (GAPHAZ, 2017), and several countries started comprehensive programs to monitor this phenomena as a basis for risk assessment (Pellet and Noetzli, 2020; Isaksen et al., 2022).

In Greenland, the scientific community still does not have a precise quantification of ~~mountain-rock wall~~ permafrost distribution. Available models are based on numerical simulations at kilometer scale (~~Daanen et al., 2011~~) (Brown, 1960; Daanen et al., 2011), are not calibrated with in-situ data (Gruber, 2012), or valid for sedimentary terrain only (Obu et al., 2019). Furthermore, our understanding of the evolution of mountain permafrost in the region is limited, as only Daanen et al. (2011) investigates future permafrost distribution, although at 25 km resolution. This knowledge gap ~~challenges our understanding~~ poses a significant challenge to our comprehension of mountain hazards and their evolution, ~~preventing a regional scale hazard assessment that Greenland urgently requires, as landslides related to permafrost degradation are common (Svennevig, 2019; Svennevig et al., 2022, 2023; W and the population is affected by these events~~ hindering the urgent need for a regional-scale hazard assessment in Greenland. This is particularly pressing due to the prevalence of landslides associated with permafrost degradation, as evidenced by prior studies (Svennevig, 2019; Svennevig et al., 2022, 2023; Walls et al., 2020), and the tangible impact of these events on the local population (Strzelecki et al., 2020).

~~A major challenge when modeling mountain permafrost in this region is due to data availability, as~~ The fact that ground temperature data in Greenland are limited to a few low-land sedimentary boreholes that are not representative for ~~higher elevation and complex terrain~~ rock wall bedrock permafrost in complex terrain, is a major challenge for modelling this feature in this region. (Obu et al., 2019). A common strategy to overcome this issue is based on the approach developed in Switzerland in the early 2000's (Gruber et al., 2004) relying on a network of permanent surface temperature loggers. These data are used for transient modelling of ground temperatures across 1D profiles in relation with depth (Westermann et al., 2016), as well as in 2D (Magnin et al., 2017) and more complex 3D geometries (Noetzli et al., 2007). Several studies model ground temperatures using numerical approaches, as TEBAL (Stocker-Mittaz et al., 2002; Gruber et al., 2004) and CryoGrid (~~Westermann et al., 2016; ?; ?; Myhra et al., 2017~~) (Myhra et al., 2017; Czekirda et al., 2023). Both models have a numerical approach to the evaluation of the Surface Energy Balance (SEB), i.e. the transfer from weather parameters to surface energy flux as upper boundary condition for the heat transfer module. Other studies have handled the SEB problem using an empirical approach based on correlating weather data and measured ground surface temperatures (Magnin et al., 2017; Etzelmüller et al., 2022; Rico et al., 2021; Legay et al., 2021). This approach has the advantage of reaching good performances while requiring only basic climatic input, i.e. air temperature and solar radiation.

~~Another challenge in modeling mountain permafrost is due to the influence of snow cover. Snow is known to cause severe disturbance to ground surface temperatures, which can significantly affect active layer thickness even when accumulating in isolated patches (?). Models are sensitive to snow characteristics (Etzelmüller et al., 2022), causing estimation of permafrost~~

extents to greatly vary depending on the modeling assumptions (?). Although some numerical models are able to describe snow physics at hectometric resolution (?), it becomes extremely challenging to achieve a good knowledge of spatial characteristics of the snow. An additional source of data used to complement modeling efforts in the context of rock wall permafrost is offered by the Electrical Resistivity Tomography (ERT). The ERT is a well-established method in rock wall permafrost research/investigations, which has been demonstrated to provide information about the electrical properties with high spatio-temporal resolution that can be interpreted in terms of the thermal state of subsurface materials (Hilbich et al., 2008; Keuschnig et al., 2017; Magnin et al., 2015). ERT data can be acquired in complex terrain, given the spatial variability of weather forcing, as wind and shading. To overcome this issue when modeling mountain permafrost, snow is often accounted with a topographical approach, based on filtering snow covered areas using a slope threshold (Magnin et al., 2019) to exclude them from the model or to apply specific offsets (Etzelmüller et al., 2022; ?). Overall, this method allows for a first order quantification of ground temperatures in complex terrain when detailed snow data are not available and gather relevant information in relatively short time (Magnin et al., 2015b;). The ERT data allow to observe frozen/unfrozen patterns in the bedrock, that can be compared to the numerical simulations of ground temperatures providing an additional source of model testing (Duvillard et al., 2020). In particular, this methodology develops a bidimensional transect of ground freezing conditions at a given survey date, which can validate 2D numerical simulations (Magnin et al., 2017; Etzelmüller et al., 2022).

The aim of this study is to move a first step towards a high-resolution regional characterization of mountain understanding the distribution patterns and future evolution of rock wall permafrost in Greenland. To do so, we focus on the Sisimiut area, (68° N on the west coast), where we have a relatively large amount of data. In fall 2020 we installed 28, we installed 9 surface temperature loggers in the area measuring Ground-Rock Surface Temperature (GSTRST), covering the local range of elevations and aspects. Using these data, we train a statistical model to evaluate the correlation between weather variables and measured GST (i.e. air temperature and incoming shortwave solar radiation) and measured RST. Weather data belong to different sources and are downscaled using a basic elevation-gradient and solar exposure approach based on a Digital Elevation Model the TopoSCALE algorithm (Fiddes and Gruber, 2014). The statistical model is then used to compute time-series of GST at any location in the landscape and for the period 1850-2022. Snow influence is modelled using a probabilistic approach quantifying presence/absence of persistent snow cover, which tunes an empirical temperature offset added to the GST time series. These time series are used as the boundary conditions for a heat transfer model. In this study, we use COMSOL Multiphysics® heat transfer module, connected to Matlab through LiveLink (COMSOL Inc., 2015). We calibrate and test our model for 1D simulation, which we compare to with temperature data obtained by two 100 m deep boreholes drilled in bedrock at low elevation in 2019 and 2021. To obtain field data on ground temperature at high elevation in mountain terrain, we used the ERT approach proposed by Duvillard et al. (2020) based on geophysical surveys and calibration of resistivity-temperature dependencies in laboratory experiments. This methodology develops a bidimensional transect of ground freezing conditions at a given survey date, which is compared to our 2D numerical simulations. Finally, we model future evolution of permafrost distribution in the area using scenarios RCP 2.6 and RCP 8.5, observing a relevant permafrost loss. Duvillard et al. (2020). We aim to answer three research questions:

1. Can our model reproduce permafrost patterns in agreement with our dataset?

2. What is the current distribution of rock wall permafrost in our study site?
3. What is the possible evolution of rock wall permafrost by the end of the 21st century under different RCP projections?

Overall, this study provides an insight on mountain-rock wall permafrost distribution in central-West Greenland, highlighting how this system is sensitive to recent and future climate changes/variability.

2 Study site

Our study site is located in the mountains surrounding Sisimiut, a city on the coastline of the widest non-glaciated area in West Greenland, about 200 km from the Greenland Ice sheet (see Fig.1). Sisimiut is the second largest city in Greenland, counting 5582 inhabitants in 2020 and experiencing a rapid development. The city is surrounded by two main mountain ridges: the Nasaasaaq – Appillorsuaq ridge to the south, summiting at 784 m.a.s.l., and the Palasip Qaqqaa– Sammisooq ridge to the north, summiting at 605 m.a.s.l. (see Fig. 1a). The landscape is characterized by narrow fjords, alpine summits and isolated coastal glaciers. The dominant lithology is amphibolitic gneiss (Ljungdahl, 1967). The mountains of the region typically have pyramid-shaped summits and steep rockwalls-rock walls generating debris slopes underneath. Mountains are dominated by bedrock, although vegetation patches are common at up to 400 m.a.s.l.

Climatically, Sisimiut is located in the low arctic oceanic area, and weather data are recorded is subject to climate data collected at the airport weather station (Cappelen et al., 2021; Cappelen and Jensen, 2021) –The warmest month is July(see Fig. 1b). The climate in this region exhibits distinct characteristics. July, with an average temperature of 6.3 °C on average); while the coldest is March(marks the warmest month, while March is the coldest at -14.0 °C). Mean annual air temperature. These climatic characteristics classify Sisimiut within the sporadic permafrost zone (Obu et al., 2019; Biskaborn et al., 2019) and morphologically active rock glaciers extend to sea level elevation (see Fig. 1a).

The climate has undergone significant changes over the years. The mean annual Air Temperature (AT) increased from -3.5 °C in during 1961-1981 to -1.8 °C in the period from 2000-2020. This shift in climate is also reflected in precipitation patterns. Mean annual precipitation decreased from 509 mm in between 1961-1981 to 422 mm in 1984-2004, year in which the which coincides with the year the rain gauge was decommissioned. Decrease in precipitation concerns both solid (mean monthly precipitation-The reduction in precipitation affects both solid and liquid forms. For solid precipitation, mean monthly levels in January-April decreased from 28 mm in 1961-1981 to 25 mm in 1984-2004) and liquid (mean monthly precipitation in June-September decreased from- Meanwhile, liquid precipitation, observed from June to September, dropped from 58 mm in 1961-1981 to 49 mm in 1984-2004) precipitation. This climate locates Sisimiut in the sporadic permafrost zone (Obu et al., 2019; Biskaborn et al., 2019) and morphologically active rock glaciers are present in the area, reaching sea level elevation (see Fig.1a). The recent climatic change on the other hand- Recent climate change is believed to have caused be responsible for significant glacial retreat in the coastal along the coast. Coastal glaciers in the area ; which lost about a fourth have lost approximately a quarter of their volume in over the past three decades (Marcer et al., 2017).

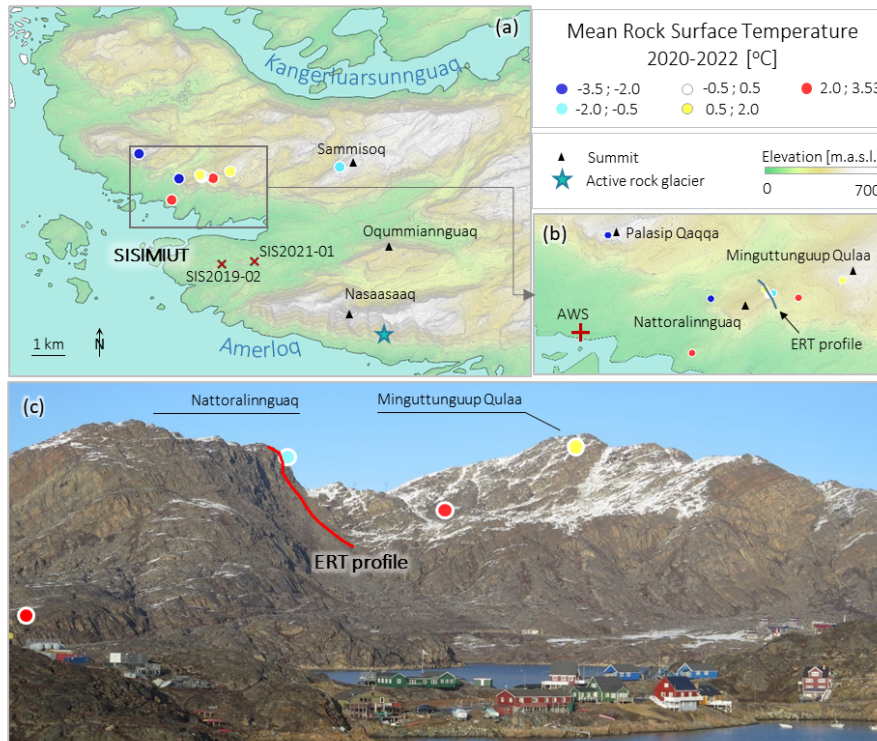


Figure 1. Study site summary. Map of the entire study area (a), with location of deep boreholes SIS2019-02 and SIS2021-01 and rock glacier fronts, identified by green stars main summits and active rock glacier. Detail of the Nattoralinnguaq area, where most of the GST-RST sensors are installed (b). South face of Nattoralinnguaq and Miguttunguup Qulaa (picture taken from Sisimiut in October 2020) with GST-RST loggers and geophysical profile locations (c). Loggers are colored based on their measured mean annual surface ground temperature-RST acquired during the acquisition period (fall 2020 to fall 2021-2022). Elevation data belong to the Arctic DEM (Porter, 2018).

3 Methods

3.1 Ground-Rock temperature monitoring

125 Ground-Rock temperatures are monitored by a network of temperature sensors installed in various settings across the study area. All sensors used for the temperature data acquisition were custom zero-point calibrated using a Fluke 7320 compact bath with a manufacturer specified temperature stability and uniformity better than 0.01 °C. The bath temperature was measured using a Fluke PRT 5610 secondary standard temperature probe, and each sensor was immersed in the bath for 40 minutes while logging every 30 seconds. After the sensor temperature stabilized, the sensor offset was calculated as $\Delta T = (\sum_{(i=1)}^n [T_{ref,i} - T_{s,i}]) / n$,
 130 where $T_{s,i}$ [°C] is the i^{th} sensor temperature measurement in the calibration period, $T_{ref,i}$ [°C] is the corresponding bath temperature measured by the PRT sensor at the same time, and ΔT [°C] is the average calculated sensor offset, which was applied as a correction to each field temperature measurement collected by that sensor.

We established a GST-RST monitoring network consisting of 28-9 individual monitoring locations, covering as evenly as possible the range of aspects, ~~elevations and slopes at the study site, and elevations of the rock walls in the study site (see Fig. 1a).~~

135 Data were acquired for ~~one year~~two years, from fall 2020 to fall 2021-2022. The technical information about loggers used are summarized in Table 1. ~~Both iButtons and~~ Geoprecisions are widely used in permafrost studies and the community has previous experience in their strength and weaknesses (Gruber et al., 2004; ?; Magnin et al., 2015a, 2019; Hipp et al., 2014; Schmidt et al., 2021; Du

~~This combination of loggers is a common trade-off between equipment costs and data quantity/quality. The iButtons are low-cost digital chip temperature sensors, which provide a reasonable temperature resolution of 0.0625°C. Our calibration~~

140 ~~show that iButtons have offsets reaching a maximum of 0.7 °C. Additionally, since they are primarily designed for indoor use, they are prone to failure when used in harsh environment. According to ?, about 5-10% of the deployed loggers can be expected to fail and protecting the logger with plastic film (as we did) helps to reduce failures. Geoprecisions on the other hand are more expensive and reliable loggers, which provide a better quality measure. According to (Gruber et al., 2004; Magnin et al., 2015a, 2019; Hipp~~

. According to our calibration, Geoprecision offsets reach a maximum of 0.10 °C. Finally, Geoprecision loggers can be accessed

145 remotely, allowing download of data within 10-20 m range, which becomes handy in steep terrain.

~~Given these characteristics, we decided to install nine Geoprecision loggers in steep bedrock, as these data are strategically more relevant in the context of the study. These loggers were placed by drilling a~~ The sensors were placed in 10 x 300 mm hole and sealing the sensor using frost-resistant resin. ~~For The iButtons (19 loggers in total), were installed in other more accessible conditions, such as flat bedrock (6), soil (11) and easy-access rockwalls (2) (See Fig. 1). In bedrock conditions, loggers were~~

150 ~~placed in 22 x 100 mm holes, sealed with a mixture of sand and frost resistant sealant. In soil conditions, loggers where placed in 50 mm holes manually dug in gravel. holes, thereafter sealed with frost resistant resin.~~

~~Two~~ While deep boreholes in rock walls are not available in our study area, we have valuable data from two 100 m deep boreholes, SIS2019-02 and SIS2021-01, ~~are which were~~ drilled in bedrock outcrops ~~in relatively on~~ flat terrain at 50 and 70 m.a.s.l. (see Fig.1) ~~and similar conditions of a).~~ While these locations differ from our primary focus on rock wall permafrost,

155 we have incorporated their data into this study and will address the associated limitations in our discussion. The boreholes are located in similar conditions regarding the exposure to solar radiation, ~~while snow conditions are different yet different snow conditions.~~ SIS2019-01 is located in a drift accumulation area and the snow depth can reach 2 m, while SIS2021-01 is on a wind-exposed hill, which ensures snow-free conditions most of the winter. Both boreholes are drilled using a Sandvik DE130 compact core drill owned and operated by the Greenland School of Minerals and Petroleum, with wireline NQ drilling tools

160 (outer diameter: 70 mm). The holes are installed with a 100 m long PE casing (outer diameter 32 mm, inner diameter 26 mm), closed at the bottom with a heavy duty heat shrink end cap with heat activated glue.

Borehole SIS2019-02 does not have a permanent sensor installed, and ~~it was logged manually three times since it was drilled. The measurement is done at 2 m depth intervals, using the available dataset consists of four temperature profiles logged manually. This was done at three distinct dates: 27 October 2020, 17 November 2020, 20 January 2021 and 9 November 2021.~~

165 For each measure we use a HOBO U12-015-02 logger. ~~The logger uses a ,~~ logging at 10 see-s sampling interval and ~~rests at each depth resting at predefined depths~~ for two minutes (see Table 1 for measuring depths). In the post processing, temperatures are averaged only over the last minute to obtain the temperature at a particular depth, thereby ensuring the sensor has equilibrated

	RST		Deep Boreholes	
Nb	4	5	1	1
Brand	Geoprecision	Maxim-integrated-Geoprecision	Geoprecision	HOBO
Type	MLog5W Rock	MLog5W Rock	MLog5W STRING	5-inch Probe
Sensor	Tnode	DS1922L-PT1000	Tnode	U12-015-02
Resolution [°C]	0.01	0.001	0.01	0.03
Accuracy [°C]	0.1	0.1	0.1	0.25
Logging interval [hrh]	1	1	1	0.00028
Sensor(s) depth [m]	0.3, 0.9	0.05-0.3	[0.1,0.5,1.0,1.5,2.0,3.0,4.0,5.0,7.5,10.0,12.5,15.0,17.5,20.0,25.0,30.0,35.0,40.0,45.0,50.0,55.0,60.0,65.0,70.0,75.0,80.0,90.0,99.0]	[1,5,10,15,20,25,30,35,40,45,50,55,60,65,70,75,80,85,90,95,97.5]
Terrain	Steep bedrock	Soil, Bedrock, Steep Bedrock	SIS2021-01	SIS2019-02

Table 1. Summary of the temperature sensors and their specifications used ~~to measure GST~~ in the study area ~~form fall 2020 to fall 2021~~.

to the new temperature. The borehole SIS2021-01 is equipped with a permanent GeoPrecision thermistor string with 28 sensors (TNode, digital chip with 0.01 °C resolution). The upper-most sensor is located at 0.1 m.b.g.s., the lower-most at 99 m.b.g.s.
 170 The sensor spacing progressively increases with depth from 0.4 m in the top to ~~10~~ 10.0 m at depth, and the logging interval is 1 hr.

3.2 Geophysical data

~~We measured a geophysical profile to~~ To obtain information on deep permafrost distribution in ~~different topographical settings than the terrain hosting the two boreholes. The profile was conducted~~ mountain terrain, we use the approach proposed by
 175 (Duvillard et al., 2020), consisting in a combination of ERT measurement on the field and laboratory experience to calibrate the temperature-resistivity relationship characteristic of the rock. The ERT measure takes place in October 2020, across the north and south faces of Nattoralinnguaq (353 m.a.s.l) ~~-(see Fig. 1b).~~ This summit presents typical characteristics of the mountains in the Palasip Qaqqā– Sammissoq ridge: a steep and rocky south face approximately 100 m high with a debris slope underneath, and a more gentle north face characterized by small vegetation patches and some short steeper sections (see Fig.
 180 1c). ~~This specific mountain was chosen for its accessibility, as the road leading to the airport passes just nearby a short path that leads to a popular viewpoint to the summit.~~

~~Electrical resistivity tomography (ERT) yields only qualitative information on the thermal state of materials because electrical conductivity depends on many parameters including water content, salinity, cation exchange capacity, and temperature.~~

The advantages of these geophysical methods are their low cost and the fact that they provide 2D or 3D tomograms/images of the subsurface. The geophysical investigations were conducted in early October 2020 using Electrical Resistivity Tomography. ~~Five~~ The ERT measure consists of one profile 450 m long (five 100 m long ~~cables (500 m long profile)~~ cables) and a total of 100 electrodes (~~deployed with 5 m spacing~~) ~~were connected to a~~. We use a 12 V external battery for powering the resistivity meter (Guideline Geo Terrameter LS2 ~~powered by a 12 V external battery~~). ~~We used~~ and injecting the current. We use 10 mm x 100 mm stainless steel electrodes, inserted in pre-drilled holes with a paste of salty bentonite to improve the galvanic contact/reduce the contact resistances and prevent freezing (Krautblatter and Hauck, 2007; Magnin et al., 2015b). ~~The Wenner configuration was used~~ For the data collection, we use the Wenner configuration because of its best signal-to-noise ratio in complex environments (Dahlin and Zhou, 2004; Kneisel, 2006). Topography was extracted from a 2 m resolution digital elevation model (DEM, Porter (2018)) based on electrode positions measured with a handheld GPS device. We cleaned 4% of the ~~data point measures~~ acquired before the inversion (549 ~~points measures~~ acquired, 528 inverted) by filtering out the outliers from the pseudo section. The data were inverted with the RES2DINV-4.8.10 software using a smoothness-constrained least-squares method and the standard Gauss–Newton method (Loke and Barker, 1996). The inversion was stopped at the third iteration when the convergence criterion was reached, i.e. when the RMSE variation versus the previous iteration is below 10%.

In addition to the field measurements, we ~~performed~~ perform a laboratory electrical conductivity experiment on ~~two rock samples collected in the field from the rockwalls on the south and north face~~ three rock samples following the procedure described by Coperey et al. (2019). These analyses define the relation between resistivity collected in the field and ~~freeze-thaw conditions of the ERT transect. The three granite cubic core samples considered for laboratory analyses~~ rock temperature, under the assumption that the material is not fractured and isotropic. The rock samples are collected from the rock walls on the south and north face (sample G-RF, G-LR and G-DA) and are characterized by a porosity of $\Phi = 0.032$ for G-RF, $\Phi = 0.015$ for G-LR and $\Phi = 0.023$ for G-DA. Before performing the laboratory measurements, ~~the samples were~~ each sample is cut in a 4 x 4 x 4 cm cube, is dried for 24 hours at 60 °C, ~~then and eventually~~ saturated under vacuum with degassed water from melted snow taken in the field. The ~~samples were~~ cubes are then left several weeks in the solution to reach chemical equilibrium. The water conductivity at 25 °C and at equilibrium ~~was is~~ 0.0118 S m⁻¹ for G-DA and 0.0142 S m⁻¹ for G-RF and G-LR. The ~~sample holder was~~ cubes are then placed in a heat-resistant insulating bag immersed in a thermostat bath (KISS K6 from Huber; bath volume: 4.5 l). The ~~temperature of this bath was controlled with internal sensor the temperature of the sample was control with external sensor with~~ bath temperature is regulated using an internal sensor with a precision of 0.1 °C, while the rock temperature is monitored with an additional sensor, also offering a precision of 0.1 °C. Glycol ~~was is~~ used as heat carrying fluid and the conductivity measurements ~~were are~~ carried out with the impedancemeter. The ~~(in-phase) conductivity measurements shown here are obtain at a frequency of 1 Hz. We moved the freezing point temperature $T_F = 0$ glycol is progressively cooled from 20 °C based on direct observations on instrumented boreholes for G-RF. The measurements with $T_F = -3$ to -13 °C reflect the fact that the measurements were made only in the downward direction of the temperatures and not in the upward direction. These analyses define the relation between resistivity collected in the field and freeze-thaw conditions of the ERT transect, stopping for 2.5 h at predefined temperatures to let the rock reach thermal equilibrium with the glycol. After the equilibrium is reached, the resistivity is measured.~~

3.3 Modeling

220 Our modeling approach is based on a mixed statistical-numerical methodology, which is conceptually similar to the study developed by Magnin et al. (2017) ~~and the modelling section in Etzelmüller et al. (2022)~~. The methodology evaluates ~~Ground Surface Temperature (GST) RST~~ time series with an empirical approach, which are then used as upper boundary conditions for a heat transfer numerical model. This modelling methodology refers to a four-steps workflow: (i) acquisition of ~~climatic weather~~ forcing data and downscaling, (ii) statistical modeling and prediction of ~~GST RST~~ data, (iii) ~~snow cover modeling and~~ 225 ~~(iv) numerical modeling of heat transfer in bedrock,~~ and (iv) model validation with field data.

3.3.1 ~~Forcing Weather~~ data and downscaling

The weather data ~~were are~~ retrieved from different sources covering different periods - summarized in Table 2. ~~Weather station data for Sisimiut are available only starting in 1958, while weather stations have been running in Nuuk (300 km south) and Ilulissat (250 km north) since 1784.~~ Our time domain is divided in three periods: (i) the historical period from 1870 to 1969, 230 (ii) the current period from 1970 to 2022, and (iii) the future scenarios from 2023 to 2100. While a weather station at the Sisimiut airport has been recording AT since 1961 (Cappelen and Jensen, 2021) (dataset d in in Table 2), it is noteworthy that such long-term data collection is rare in most areas in Greenland. Consequently, we have chosen to utilize weather data available at the regional scale to force our model, and keep the Sisimiut weather station data as validation set. This choice allows us to understand the modeling uncertainties inherent in regional-scale weather data, with the broader aim to assess how 235 this methodology could be applied in other areas of the region. Therefore, we ~~generated a custom dataset for Sisimiut covering the period prior to 1958 (dataset a~~ evaluate the performance of each of the following dataset by comparing their AT to the data from the Sisimiut weather station over the overlapping period.

The weather data for the current period are obtained from the ERA5 reanalysis, that we downloaded from the Copernicus database (Hersbach et al., 2020) (dataset b in in Table 2). For ~~air temperature, we evaluated the regression between data from~~ 240 ~~Nuuk~~ this study, we use the AT at pressure levels from 1000 hPa to 500 hPa and Shortwave Solar Radiation Downwards (SSRD) at the surface level. The time series are downscaled using the TopoSCALE algorithm (Fiddes and Gruber, 2014). TopoSCALE models surface AT by interpolating the AT profile at the different pressure levels. SSRD is donwscaled by evaluating the topographical shading effect on the SSRD. The elevation data are obtained from the Arctic DEM at 10 m resolution (Porter, 2018). In order to optimize the computation time, we use the TopoSUB algorithm to optimize the computation 245 of the terrain parameters in the complex topography of our study site (Fiddes and Gruber, 2012).

The AT data for the historical period are computed using AT recorded in Nuuk (300 km south) and Ilulissat (250 km north) (Cappelen et al., 2021) (datasets e1 ~~and e2~~ in in Table 2). To downscale the data, we compute the regression between these time series and the downscaled ERA5 time series over the overlapping period (1970 to 2022) ~~over the overlap period 1958-2022 with weather data from Sisimiut (dataset e3)~~. The regression is then used to generate ~~air temperature AT~~ for the period ~~prior to~~ 250 ~~1958.~~ For solar radiation 1870 - 1969. For SSRD, weather stations in Nuuk, Ilulissat and Sisimiut ~~did do~~ not have this variable measured. ~~We~~ For this dataset, we generated a synthetic ~~estimation SSRD estimation~~, equal to the average year over the period

Dataset reference	Label	Period Available	Period used	Variables
Custom made	a	1784-2021	1870-1959	Air tempertaure -temperature Solar radiation
Herbasch et al 2019	b	1979-present - 1970-present	1979-2022 - 1970-2022	Air temperature, solar radiation, cloud cover, dew point, wind speed/direction
Hofer et al 2020; Bentsen et al., 2013, RCP 2.6	c	2006-2100	2022-2100 - 2023-2100	Air temperature, solar radiation
Hofer et al 2020; Bentsen et al., 2013, RCP 8.5	d	2006-2100	2022-2100 - 2023-2100	Air temperature, solar radiation
*Used to generate air temperature of dataset a				
Cappelen et 2021a	e1	1784-2021		Air temperature
Cappelen et 2021a	e2	1784-2021		Air temperature
Validation Dataset				
Cappelen et 2021b	e3-d	1958-2021 - 1961-2021		Air temperature

Table 2. Summary of ~~elimate~~-~~the weather~~ databases used to cover the investigation period (~~1850-1870~~-2100). ~~Datasets~~-~~Dataset a and is used to describe historical weather.~~ Dataset b ~~are is~~ used ~~for modelling present-day ground temperatures~~ to describe current weather. Datasets c and d are used for simulating scenarios RCP 2.6 and RCP 8.5 respectively. Datasets e1, e2, and ~~e3-b~~ are used to model ~~air temperature-AT~~ in Sisimiut for dataset a-. ~~Dataset d is used as long-term weather station-AT validation data.~~ ~~Dataset b is used to calibrate the RST model (See Sect. 3.3.2).~~ Datasets a, b, c, and d are ~~not available at this location~~ used to force the heat transfer simulations (See Sect. 3.3.3)

~~1979-2022~~ retrieved from global reanalysis model (dataset b). The other datasets, b to d, are publicly available and ready to use. ~~Dataset b was downloaded from the Copernicus database (Hersbach et al., 2020), and we selected the standard set of predictor variables used by CryoGrid-SEB module (Westermann et al., 2016).~~ ~~1970-2022~~ retrieved from the downscaled ERA5 dataset.

255 For future scenarios, we ~~used~~-~~use~~ the Norwegian Earth System Model version 1 (NorESM1) global circulation model, using Representative ~~Concertation~~-~~Concentration~~ Pathway (RCP) 2.6, and RCP 8.5 for 2006-2100 (Bentsen et al., 2013). The NorESM1 model is ~~also chosen by several~~ developed to focus on polar climate and is chosen by other authors in Greenland for cryosphere evolution modelling due to its good performance in the region (~~Colgan et al., 2016; ?~~) thanks to his good ~~performance in the region (?)~~ (Colgan et al., 2016). The RCP 2.6 is the NoreESM1 outcomes for scenarios of declining emis-
260 sions since 2020 (optimistic scenario, dataset c ~~in Table 2~~), while the RCP 8.5 is simulated with unregulated emissions increasing at a rate compatible to the present-day industrial development (pessimistic scenario, dataset d ~~in Table 2~~). ~~To downscale the data, we compute the regression between these time series and the downscaled ERA5 time series over the overlapping period (2006 to 2022).~~

~~Air temperature and solar radiation are downscaled at any location in our study area using a topographical approach.~~
265 ~~The downscaling depends on two parameters: elevation and potential incoming solar radiation (PISR). Elevation is used to downscale air temperature by applying a constant lapse rate of $0.047\text{ }^{\circ}\text{C m}^{-1}$, measured on the study area by the Mean Annual Ground Surface Temperature (MAGST) monitoring network by detrending the data for slope aspect and snow cover. The elevation data are obtained from the Arctic DEM at 10 m resolution (Porter, 2018). Solar radiation forcing is downscaled using the ratio between the PISR at each logger location and the PISR at the ERA5 reference grid. The PISR map is evaluated using~~
270 ~~the software System for Automated Geoscientific Analyses (SAGA) and the module PISR (?).~~

3.3.2 RST Modeling

3.3.3 **GST Modeling**

In this step, we model the relationship between forcing and GST downscaled weather data and RST data using a **data-driven** approach. Here, we use snow-free GST data collected in bedrock, as snow cover effects will be modelled in the next step. Previous studies used an offset-based approach based on the evaluation of a constant thermal offset between air temperature and snow-free GST (Magnin et al., 2017; Etzelmüller et al., 2022). In our study, we use a conceptually identical approach, based on the following hypothesis (Magnin et al., 2019): the snow-free GST can be to Magnin et al. (2019). The RST is predicted by an empirical model trained using available forcing variables that dominate GST RST distribution on steep bedrock rock walls, i.e. AT and SSRD. To do so, we aggregate each snow-free GST RST measurement to the forcing data that occurred during that acquisition time step, downscaled at the logger location. While GST RST data from the period 2020-2021-2020-2022 aggregated at monthly time steps are used as dependent variable, the climatic datasets overlapping on the same periods are used as predictors. Datasets a, c and d (see Table 2) are fitted to the GST data using air temperature and solar radiation as predictors. For dataset b, we also use cloud cover, dew point temperature, total precipitation, wind speed and direction as additional predictors. As predictors, we use AT and SSRD from the ERA5 dataset downscaled at the respective logger location. This creates a database of $N \times 1$ targets and $N \times M \times N \times 2$ data points, where N is the number of available GST data and M is the number of climatic predictors used. We then split this database into training and validation sets, following a pseudo-randomized cross validation approach, as we randomly exclude entire GST time series from training. We choose a multinomial linear model RST data.

The RST is modelled using a multinomial linear regression, trained with the Matlab function fitlm.

290 3.3.3 **Snow cover modeling**

In order to model snow cover, we develop a methodology based on constant offset similar to Etzelmüller et al. (2022). We first evaluate the average temperature offset due to snow cover by comparing the mean annual GST of sensors that were To evaluate the validation performance, we follow the classic cross validation approach that iteratively splits the dataset randomly in 80% training and 20% validation, until all datapoints are used both as training and validation. To evaluate the test performance, we predict the RST time series at the borehole SIS2021-01 location and compare it to the data measured at 0.1 m depth, which is not used for the training/were not snow covered during the entire winter 2020-2021. This offset then is multiplied to the local probability of snow cover presence/absence, that we call SnowP, varying from zero (absence of snow cover) to 1 (presence of long lasting snow cover). We compute the SnowP by training a neural network classifier with a categorical variable describing presence/absence of snow at specific locations, and topographical data describing slope angle and curvature (planar, longitudinal and profile – obtained with the morphometric features module in SAGA, ?) at those locations. This dataset is created by interpretation of 5 landscape pictures of the study area taken at the peak of the snow accumulation season (late April) in winters 2021 and 2022. We manually assigned snow/no snow areas in a GIS and combined this dataset to terrain parameters to train a binary classifier. The classifier provides a probability of snow cover for a given set of curvature and slope,

which can be extrapolated at the landscape scale creating a map of snow cover probability SnowP (Fig.??). The map identifies drift traps where snow is most likely to accumulate. The validity of this method is based on the observation that snow drift patterns in the arctic are generally stable over time due to relatively dry and windy weather (Parr et al., 2020) [validation routine](#).

Comparison of a field picture of the north face of Nasaasaq (a) taken in May 2021 from the summit of Oqummianguaq and the SnowP map (b, 3D visualization). The SnowP map identifies snow free steep terrain (1), steep chutes, drift traps, that are mostly snow covered (2) and gentle terrain features that are snow free because of snow drift (3).

3.3.3 [Heat transfer model](#)

3.3.4 Numerical modeling of heat transfer

~~Heat transfer is simulated in To describe deep rock temperatures, we develop a 1D conditions for model calibration and large scale mapping, while 2D simulations are restricted to areas of interest for more detailed analysis~~ [numerical model that we calibrate with SIS2021-01 borehole data](#). The heat transfer process is modelled using the “heat transfer in porous media” module in COMSOL, which assumes the local thermal equilibrium hypothesis to be valid [and simulates conduction only](#). The model [geometry consists in a 100 m 1D model. The model](#) accounts for three materials: solid matrix, fluid and solid with phase change. The fluid phase is the default COMSOL “water” material, to which we assigned a phase change to ice at 273.15 K and transition interval to ice of 5–2 K, according to Noetzli and Gruber (2009). ~~Since we do not have precise information on ground thermal properties, the porous matrix material is assigned as the default crystalline rock “granite” $K = 2.9 \text{ W m}^{-1} \text{ K}^{-1}$ and $C_p = 850 \text{ J kg}^{-1} \text{ K}^{-1}$. A quick sensitive analysis shows that the model computes ground temperature differences smaller than $0.01 \text{ }^\circ\text{C}$ when varying these parameters within the typical ranges of different crystalline rocks. For the 1D model we entered a custom function to describe the matrix density, which was evaluated from the cores extracted from~~ [The matrix density is assigned in agreement to the data from the core extracted from SIS2021-01, providing an empirical function of depth increasing. The data show an increase from \$2600 \text{ kg m}^{-3}\$ at the surface to \$3000 \text{ kg m}^{-3}\$ at 20 m depth, and being constant until 100 m depth. We attributed the constant density of \$3000 \text{ kg m}^{-3}\$ to the 2D models, as it not known if the near-surface values measured at b.g.s., and then remaining constant thereafter.](#)

~~Since we do not have precise information on the rock thermal properties, we calibrate the specific heat capacity, thermal conductivity and matrix porosity of the solid phase. The calibration is carried out by simulating conditions in SIS2021-01 are representative for the entire study area, from 1870 to 2022 using a 1D geometry of a 100 m column. The simulation results are then compared to the field data acquired during the period August 2021 to April 2022. This is repeated for different combinations of thermal properties, targeting the minimization of the RMSE between the measured and modelled temperatures across the borehole depth.~~

The numerical simulation consists of ~~four~~ [three](#) successive studies: a stationary study for initial conditions (mean conditions for ~~1850–1860~~ [1870–1890](#), forcing dataset a), a transient study ~~1850–1979–1870–1969~~ [\(forcing dataset a\)](#) ~~and~~ [a transient study 1979–2022–1970–2022](#) (forcing dataset b) ~~and a transient study 2022–2100, depending on the scenario chosen (RCP 2.6 and RCP 8.5 – forcing datasets c, d). For each time period (1850–1979; 1979–2022 and 2022–2100), the corresponding GST model and~~

forcing time series are stored in COMSOL as analytical functions using local elevation, PISR, SnowP and time as parameters that can be modified by the user to reproduce ground temperatures in different topographical settings. Therefore, by entering custom local topographical conditions, the GST model will produce downscaled GST time series that are imposed as upper boundary conditions for the COMSOL heat transfer module. All weather datasets are downscaled at the desired location using the TopoSCALE algorithm, as described in Sect. 3.3.1. The corresponding RST time series is computed using the RST model developed in Sect. 3.3.2 and used as surface boundary condition.

As lower boundary condition, we impose the constant geothermal heat flux, which we also evaluated from the SIS2021-01 data. Our data indicate a temperature gradient of $0.015 \text{ }^\circ\text{C m}^{-1}$, which, considering a thermal conductivity of $2.9 \text{ Wm}^{-1}\text{K}^{-1}$, gives a constant geothermal heat flux of 0.045 Wm^{-2} .

3.3.4 Model calibration

The numerical model is calibrated for two parameters: matrix porosity and initial conditions in 1850. The calibration is carried out by simulating conditions in SIS2021-01, from 1850 to 2022 using a 1D geometry of a measured from 100 m column. The simulation results are then compared to the field data acquired during the period August 2021 to April 2022. This is repeated for different combinations of matrix porosity and initial conditions, aiming to minimize the difference between data and model results. For boundary conditions, we use the measured GST at the location of SIS2021-01 scaled to the local climatic variables over the period 1850-2022. For downscaling, we evaluate elevation and PISR on the respective raster maps (elevation = 77 m.a.s.l., PISR = 790 kWhm^{-2}). At this location the SnowP map fails to describe snow conditions that we observe on the field, and we manually impose the value of SnowP = 0.3 at this stage. We test different porosity values according to previous studies findings and field measurements, i.e. porosity ranging from 0.01 (Rico et al., 2021) to 0.05 (Magnin et al., 2017). to 90 m.b.g.s. at SIS2021-01. As initial conditions, we compute the temperature profile of the stationary solution of the 1D model forced by the average GST RST over the period 1850-1870 - 1860-1890. We then add a positive ground temperature offset as parameter to account the fact that temperatures in 1850-1860-1870 - 1890 (at the Little Ice Age peak) were lower than the previous period, and deep ground temperatures were likely higher than modelled by our stationary model. The optimization of the two parameters targets the best fit between measured and modelled temperatures below the depth of zero annual amplitude. This temperature offset is also matter of calibration.

3.3.4 Mapping ground temperatures

The ground temperature map is computed by evaluating the calibrated

3.3.4 Model testing

To test the performance of the numerical model, we simulate rock temperatures using the calibrated thermal characteristics and RST boundary conditions downscaled at the SIS2019-02 and the ERT profile locations. The former simulation is set up using the 1D model for each set of topographical condition in our study area. This process is handled by Matlab's LiveLink, which

runs the routine through each gridcell in the DEM, PISR and SnowP maps, and passes the local topographical parameters to the 1D COMSOL model. The COMSOL studies are run through Matlab command and the export is stored in a text file which contains the evolution of temperature in the 1D model over time for each gridcell. Considering that the depth of zero annual amplitude measured at the borehole locations is approximately 10-20 m, we compute the mean ground temperature (2012-2022) at 20 meters depth (MGT20) as a proxy for mapping permafrost presence. Matlab imports the output at each loops and stores the MGT20 and assigns it to the corresponding raster cell, creating the MGT20 map geometry described in the previous section. The latter simulation is set-up using a 2D geometry along a north-south transect extracted from the DEM using QGIS (Quantum GIS, (QGIS, 2023)). The elevation profile is then imported into COMSOL as 2D geometry using the parametric function option. We then evaluate the RST forcing independently at each profile node using the approach described in Sect. 3.3.2. The RST time series are then parameterised as function of the spatial variable (x) and temporal variable (t), and used as surface boundary condition for the 2D model. As lower boundary condition, we impose the geothermal heat flux evaluated from the borehole SIS2021-01, while we impose zero-flux conditions on the lateral boundaries.

3.3.5 2D Models

~~The use of a 1D model~~

3.4 Permafrost distribution and evolution

In this last section, we explore the present and future distribution of rock wall permafrost in the study area using the modeling tools we have developed in the previous steps. At first, we use the RST model to compute rock wall temperature maps. This allow us to visualize the potential distribution of rock wall permafrost. To do so, we first define the rock walls from the DEM as terrain steeper than 40 degrees (Magnin et al., 2019). In the study site, 9.32 km^2 are steeper than 40° and classified as rock walls. For each grid cell that qualifies as rock wall, we then compute the RST time series by predicting the RST model on the downscaled AT and SSRD time series for both the current period and the future scenarios. The rock wall temperature maps are then computed by evaluating the Mean RST (MRST) for the ~~mapping module disregards lateral influences, and we expect our map to be imprecise in~~ period 2002-2022 and for the period 2080-2100 using both scenarios RCP 2.6 and RCP 8.5.

In our second analysis, we focus on predicting the future evolution of deep rock temperatures at the SIS2021-01 location. Given that our numerical model is calibrated to fit the data collected at this very site, the ~~proximity of sharp slope breaks and ridges. 2D models on the other hand provide a much stronger approximation~~ level of uncertainty here is arguably at its minimum. To do so, we append a two independent transient studies to the heat transfer model generated in Sect. 3.3.3. As upper boundary condition, we use downscaled RST time series for the two climate scenarios (RCP 2.6 and RCP 8.5, datasets c and d in Table 2) from 2023 until 2100. We then compare the generated temperature profiles for 2100 and describe the permafrost evolution at this site.

In our last analysis, we assess the evolution of mountain permafrost in complex terrain, ~~as they provide similar results for 3D transient simulations (Noetzli et al., 2007). For this reason, we compute using a 2D model for two location of special interest~~ modeling approach. Our investigation centers on two specific locations: the ERT profile and the Nasaasaaq summit

~~The first location transect and the Nasaasaq summit ridge. The latter site is chosen to compare the ERT data to our model, while the second location allows us to model and understand permafrost distribution and evolution in the tallest mountain in the study observe the expected evolution of rock wall permafrost at the highest elevations in the area. For each location we set up a north-south transect in the QGIS software, and used it to sample the elevation profile from the DEM. The elevation profiles are then imported into COMSOL as both locations, we employ 2D geometry using the parametric function option. The same method is used to import PISR and SnowP along the transects. In this way, we can provide the GST model as an interpolation function over the spatial variable (x) and temporal variable (t): $GST(x, t) = f(z(x), PISR(x), t) + dT \cdot SnowP(x)$, where f is the linear GST models for each forcing dataset. As lower boundary condition, we impose the geothermal heat flux of 0.045 Wm^{-2} evaluated from the borehole SIS2021-01, while we impose zero flux conditions on the lateral boundaries. models driven by RST time series from 1870 to 2100, which have been downscaled along the elevation profiles following the methodology outlined in Sect. 3.3.4. We conduct the heat transfer model simulations for both RCP scenarios, allowing us to compare their different impacts on rock wall permafrost~~

4 Results

3.1 Ground temperature monitoring

4 Results and Discussion

GST

4.1 Rock temperature monitoring

~~RST data are measured during one full year two full years, as loggers were installed in September-October September - October 2020, and retrieved one year later, and data collected in September - October 2022. Most loggers show sub-zero GST RST between early October and late May. Fifteen loggers present snow-free GST data (Fig. ??a), seven present thick snow cover and six present intermediate characteristics (Fig. ??b). In general, snow cover onsets in early November and lasts until mid-June, although this depends on the specific logger location. Lowest GSTs Lowest RSTs are reached in late March, when several loggers recorded temperatures around $-20 \text{ }^\circ\text{C}$ (see Fig. ??2a). The lowest GST (-22.8 RST ($-21.2 \text{ }^\circ\text{C}$) is recorded on March 28 25 February 2022 by a logger installed on a north facing bedrock slope at 476 314 m.a.s.l.. Highest GSTs RSTs are reached at the end July, as several loggers recorded temperatures above $25 \text{ }^\circ\text{C}$. The data show that mean annual ground surface temperature (MAGST) MRST is correlated with elevation and aspect mean SSRD (see Fig. ??e and d2b). To show the effect of elevation, we compare two snow-free loggers installed on south facing rockwalls, one at sea level (MAGST 52 m.a.s.l. (MRST = $+3.5$ $3.2 \text{ }^\circ\text{C}$) and at 460 522 m.a.s.l. (MAGST MRST = $+1.2$ $0.6 \text{ }^\circ\text{C}$), giving a MRST gradient of $0.0055 \text{ }^\circ\text{C m}^{-1}$. By comparing loggers installed on rockwalls rock walls at the same elevation but on opposite aspects, we obtain a MAGST MARST offset of $2.2 \text{ }^\circ\text{C}$ from north to south facing slopes.~~

Boreholes temperatures are shown in Fig. ?? ~~In SIS2019-02, the depth~~2b and Fig. 2c. SIS2021-01 (see Fig. 2c) shows consistently negative temperatures between 20 and 70 m depth, reaching a minimum of $-0.2\text{ }^{\circ}\text{C}$ at 30 m depth. The depth of zero annual amplitude is approximately ~~20 m.~~~~Below 10 m.b.g.s..~~ Since we measure negative temperatures below this depth, the data from SIS2021-01 indicate the presence of permafrost. In SIS2019-02 (see Fig. 2d), temperature data indicate a minimum of temperature of $+0.3\text{ }^{\circ}\text{C}$, reached at 30 m depth, and a temperature of $+1.0\text{ }^{\circ}\text{C}$ at 100 m. ~~The depth of zero annual amplitude is approximately 20 m.~~ Since temperatures are positive below the depth of zero annual amplitude, the measurements at SIS2019-02 indicate absence of permafrost.

In comparing the contrasting conditions between SIS2019-02 and SIS2021-01, it is important to note that SIS2019-02, situated at the same elevation and in a slightly more shaded location than SIS2021-01 ~~shows consistently negative temperatures between 20 and 70 m depth, reaching a minimum of $-0.2\text{ }^{\circ}\text{C}$ at 30 m depth. The depth of zero annual amplitude is approximately 10 m. b. g. s. .~~ Since we measure negative temperatures below this depth, the data from ~~exhibited lower solar radiation levels ($90\text{ }Wm^{-2}$ versus $104\text{ }Wm^{-2}$) during the period 1970-2022. Given this difference, one might anticipate that SIS2019-02 would display permafrost conditions, as observed in SIS2021-01~~ indicate the presence of permafrost. We propose that the temperature data indicate that the presence or absence of permafrost is influenced by the distinct snow cover characteristics at these two sites. In arctic climates, snow drifts often form early in the season, and these drift patches persist across different seasons (Parr et al., 2020). The early onset of snow cover has a warming effect on the ground, and when this pattern recurs each winter, as is suspected to occur in SIS2019-02, it can result in a warmer ground compared to a wind-exposed area such as SIS2021-01.

Overall, the temperature data delineate discontinuous permafrost conditions in rock walls and bedrock. Given the range of elevation where permafrost is found, this conditions are similar to those described in Northern Norway ($69 - 71^{\circ}\text{ N}$), where negative MRST and rock wall permafrost can be found at sea level on north facing slopes (Magnin et al., 2019). This offset is known to be dependent on latitude, varying from $8\text{ }^{\circ}\text{C}$ in the European Alps ($45-46^{\circ}\text{ N}$, Magnin et al. (2015a)) to $1.5\text{ }^{\circ}\text{C}$ in Northern Norway ($69-71^{\circ}\text{ N}$, Magnin et al. (2019)). In coastal climates, previous studies suggested that steep bedrock permafrost could be influenced by other factors than pure solar radiation, as cloudiness and icing, creating an abnormally low offset in New Zealand (Allen et al., 2009). Despite the fact that the Sisimiut mountain area is coastal, our data suggest that this process is not a relevant factor for rock wall distribution in the area.

~~Data and model comparison for boreholes SIS2021-01 (a) and SIS2019-02 (b). For borehole SIS2021-01, data are acquired with an interval of 1 hr using a MLog5W-STRING, allowing us to color plot temperatures as function of depth and time. Data are compared to model results—see section 4.3.3. For borehole SIS2019-02, data were measured on four separate dates, using a 5-inch Probe lowered manually into the borehole. These measurements produce four temperature profiles, i.e. temperature as function of depth, that are compared to the model results.~~

4.2 Geophysical survey

~~As shown in Fig.3b, the electrical conductivity tomograms acquired show a vertical and also lateral variations distribution of the conductivities with low conductivity values ($< a$, the conductivity values measured along the profile vary from values~~

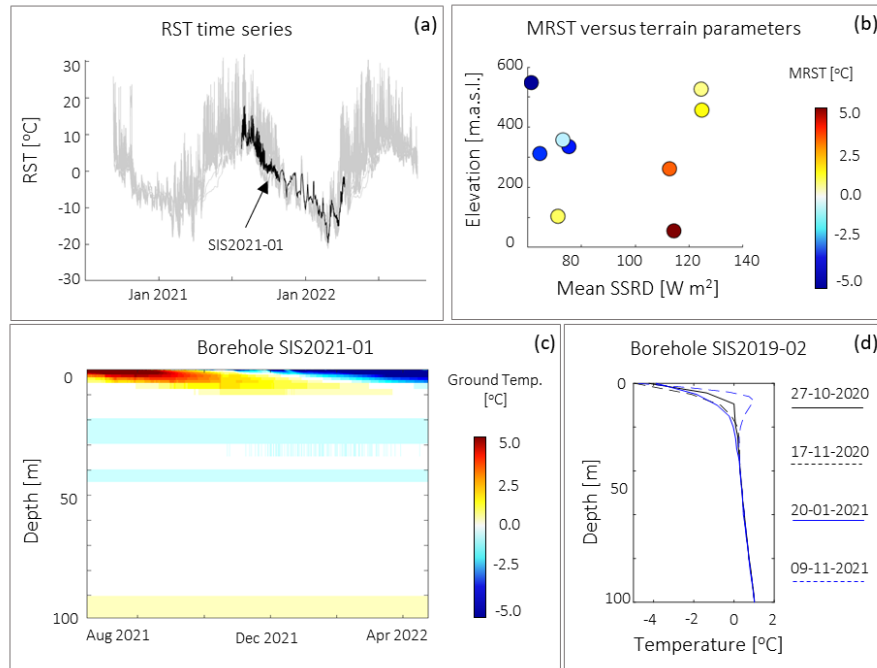


Figure 2. Summary of GST-temperature recorded by the loggers during 2020-2021-2020-2022. On top, examples of GST-RST time series are for a snow-free logger all loggers (a) and snow-covered logger. In black, is shown the RST recorded at SIS2021-01; this dataset is used as test set for the RST model (b See Sect. 3.3.2). On bottom, Relationship between MRST recorded during the MAGST observational period (2020-2021) in relation to topographical predictors predictor Elevation and mean SSRD during the observational period (b). Temperature data from boreholes SIS2021-01 (c) and Potential Incoming Solar Radiation SIS2019-02 (d). For borehole SIS2021-01, data are acquired with an interval of 1 hr using a MLog5W-STRING, allowing us to color plot temperatures as function of depth and time. For borehole SIS2019-02, data were measured on four separate dates, using a 5-inch Probe lowered manually into the borehole. These measurements produce four temperature profiles, i.e. temperature as function of depth.

465 below $10^{-3.5-2} \text{ Sm}^{-1}$) below the north and south face and high values inside the mountain (\rightarrow up to $10^{-4.4-6} \text{ Sm}^{-1}$). The
 . According to the petrophysical analysis, shown in Fig.3a, highlights a transition zone from frozen to thawed conditions b,
 this range of conductivity highlights the co-existence of frozen and unfrozen conditions. Although the precise relationship
 temperature - conductivity is dependent upon the single sample, the analysis shows a common pattern of sharp increase in
 conductivity as soon as $0 \text{ }^\circ\text{C}$ temperature is reached. This feature occurs between $10^{-4.4}$ and $10^{-3.5} \text{ Sm}^{-1}$. This indicates that
 470 permafrost presence is restricted inside the mountain and close to the surface in the north face and the upper part of the south
 face. A large portion of the north face appears unfrozen for all samples. Therefore, this range of conductivity values is used as
 thresholds to define frozen, unfrozen and transition zones in the ERT tomogram. In the transition zone, our analysis is not able
 to discern between frozen and unfrozen conditions.

475 When applying these thresholds to the ERT field data, we can describe the patterns of frozen and unfrozen conditions of the mountain (See Fig.3a). Frozen conditions occur in the central section of the north face, at 300 - 350 m.a.s.l.. The frozen area reaches depths well below the depth of zero annual amplitude, indicating the presence of permafrost at this location. The summit and most of the south face are in transitioning conditions, indicating warmer temperatures than the central section of the north face. The south face is also characterized by a large unfrozen body, which we interpret as absence of permafrost in the rock wall.

480 Unfrozen conditions are also shown on the lower section of the north face, below 300 m.a.s.l.,~~occurring at the same location of a~~. The presence of unfrozen conditions at this location is in contrast with our understanding of permafrost distribution in the area. Permafrost is expected to exist on north facing steep terrain already at low elevation, as highlighted by RST and borehole data described in the previous section. Additionally, since this location is characterised by north facing aspect and higher elevation compared to SIS2021-01, we would expect colder conditions than the data collected from the borehole.

485 Although snow may play a warming role as observed in SIS2019-01, this section of the face has slopes that guarantee snow free conditions thorough the winter. To explain this anomaly, we highlight that this area coincide with a large lithological fault observable on the field. As result, the ERT tomogram shows a sharp transition in conductivity values. We suggest that the ERT data at this location are strongly influenced by other factors than bedrock temperature, such as weathering and dense fracturing. These factors challenge the isotropic conditions that are necessary to meaningfully compare laboratory analyses

490 to the ERT tomogram. All considered, we consider the ERT data at this location to be unreliable and we disregard this area of the tomogram in our further analyses.

Overall, the geophysical survey indicate that, at this location, permafrost is discontinuous. Up to this elevation (400 m.a.s.l.), the data describe either frozen or unfrozen conditions depending upon we are on a north or south facing rock wall respectively. This observation is in agreement with the RST data described in the previous section. The co-existence of frozen, unfrozen and

495 transitioning conditions suggest that deep permafrost has temperatures close to thawing point. This is in agreement with the borehole data described in the previous section.

4.3 Modeling

4.3.1 ~~GST Model~~

~~GST modeling is done at monthly time steps by aggregating weather forcing and on snow-free loggers data collected on~~

500 ~~bedrock (13 loggers available), averaged over monthly periods. The training results of the GST models are summarized by period~~

4.3.1 Weather data and downscaling

A sample time series of the available weather data is shown in Fig.4a, while the validation scatterplots of the AT data are shown in Fig.??. ~~For all datasets, we achieve similar performance in both training and validation sets, indicating good generalization~~

505 ~~power of the model. The prediction performance is best for dataset b ($R^2 = 0.98$ and $RMSE < 1.6$)~~ 4b. The validation indicate

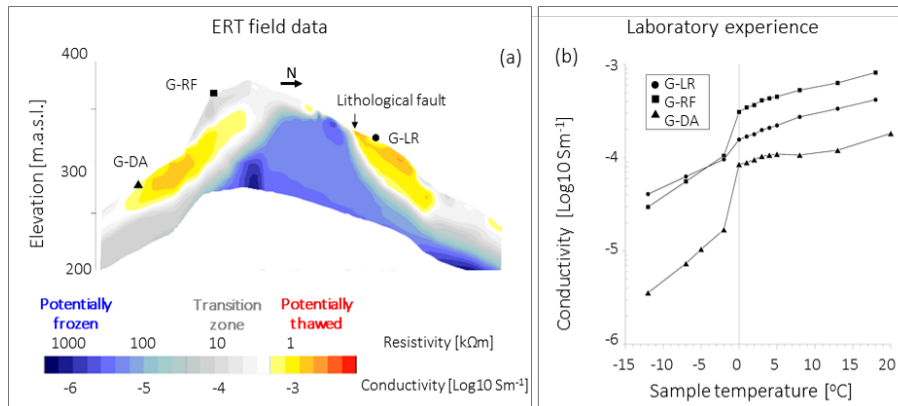


Figure 3. Comparison between ERT and 2D thermal model. a) Petrophysical analysis, showing in-phase electrical conductivity data versus temperature for Summary of the three samples collected along the geophysical profile; b) profile survey. Profile of electrical conductivity/resistivity tomography (in Sm^{-1} and $\text{k}\Omega\text{m}$) measured on the field. c) (a) resulting 2D numerical model of. Petrophysical analysis, showing electrical conductivity data versus temperature for the ridge where three samples collected along the ERT line was conducted geophysical profile (b).

a RMSE of $0.95\text{ }^{\circ}\text{C}$ between the AWS AT data and the ERA5 AT downscaled at the weather station location. This value is comparable to previous studies using this dataset in Greenland (Delhasse et al., 2020) and in complex terrain when downscaled with TopoSCALE (Fiddes and Gruber, 2014). The historical database has a similar performance, showing a RMSE of $1.28\text{ }^{\circ}\text{C}$.

510 The data from the NorESM1 scenarios have higher RMSE, indicating a poorer fit between the data and model. We believe this is an intrinsic characteristic of the model, as the mean errors between measured and modeled AT is consistent with the average error over continents declared by Bentsen et al. (2013), i.e. $-1.09\text{ }^{\circ}\text{C}$; while it is lower for the other datasets, reaching RMSE 2.38. This indicates that the dataset, when compared to historical data, tends to underestimate land temperatures.

515 It is important to notice that this analysis quantifies the performance of the AT data at sea level. Since our study evolves in complex terrain, a comprehensive evaluation of the weather database requires weather data at different elevations and including SSRD. Since we do not possess such data, we refer to the work from Fiddes and Gruber (2014) indicating that the TopoSCALE algorithm provides consistent performance across complex terrain. This suggests that we should expect similar data quality at different elevations and aspects. However, a detailed description of this source of uncertainty remains missing at this location.

4.3.2 RST Model

520 The training, validation and test results of the RST model are summarized in Fig.5. The model has consistent performance in training, validation and test, described by a stable RMSE ranging from $1.99\text{ }^{\circ}\text{C}$ to $2.66\text{ }^{\circ}\text{C}$. On average, the presence of snow cover causes an offset on the MAGST of $+1.58\text{ }^{\circ}\text{C}$. To better contextualize this performance, we compare our model to Schmidt et al. (2021) which represents the state of the art of RST modeling in the arctic. Their approach is based on the SEB

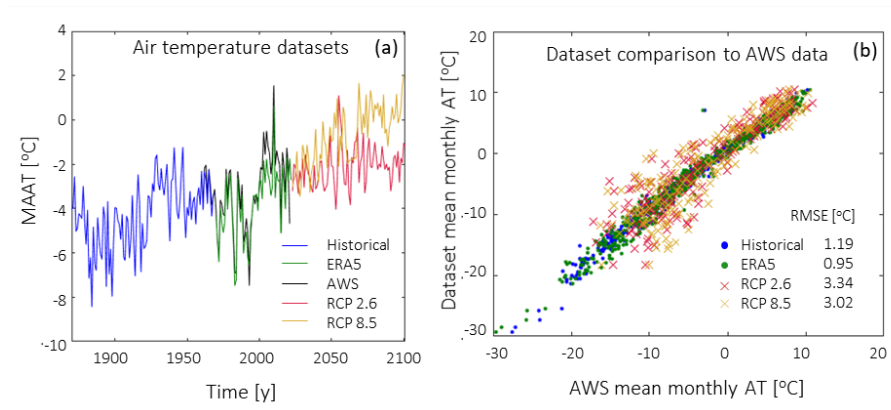


Figure 4. Weather data summary. Yearly time series of the different AT datasets, downscaled at the weather station location (a). Comparison between AWS AT and downscaled datasets AT during the overlapping periods (b).

525 module of CryoGrid 3, modified to account for vertical terrain, including vertical moisture transport affected by latent heat flux and skyview factor adapted to steep terrain. By comparing model runs and field data, Schmidt et al. (2021) obtained R^2 above 0.97 and RMSE below $1.20 \text{ }^\circ\text{C} \pm 0.41$ on monthly RST data. This value indicates a better performance than our model. This is likely due to their use of a more sophisticated model, as well as in-situ weather station data as forcing AT. For sake of comparison, if we force our model with AT from the local AWS, we obtain a lower RMSE, i.e. $1.46 \text{ }^\circ\text{C}$ when other conditions do not change ($R^2 = 0.81$). We used this value of $+1.58 \text{ }^\circ\text{C}$, comparable to previous findings in Greenland (?), as constant offset when modeling snow cover indicating that part of our RMSE is due to the uncertainty of the weather forcing. While it is possible in principle to utilize weather station data to drive our model and enhance its performance, our preference is to evaluate the model performance and associated uncertainties using regionally available data.

530

4.3.3 Heat transfer model

The model was calibrated by optimizing two parameters: matrix porosity and initial offset value. The optimal porosity was achieved for a value of 0.03 results of the heat transfer model calibration and validation are summarized in Fig. 6. The calibration of the heat transfer model indicated that the model is mostly sensitive to the porosity value, in agreement to Noetzli and Gruber (2009). According to their study, porosity dominates the sensitivity on short time scales (e.g. decades), while the matrix thermal parameters dominate the sensitivity on longer time scales (e.g. millennia). The calibration yielded an optimal porosity value of 1.5%, while the optimal initial offset was evaluated at determined to be $+1.8 \text{ }^\circ\text{C}$ with respect to the average temperature on the period 1850-1860. Using these values, the model reaches a good agreement of the seasonal frost and heat penetration depths at relative to the MRST during the period 1870-1890. The thermal parameters were initially set to the default crystalline rock matrix in COMSOL: $K = 2.9 \text{ W m}^{-1} \text{ K}^{-1}$ and $C_p = 850 \text{ J kg}^{-1} \text{ K}^{-1}$. These initial values provided the minimal difference between model run (Fig. 6a) and SIS2021-01 for the period August 2021—April 2022 data (Fig. ??a). The difference (6b) that we managed to achieve. Consequently, we maintain these parameters unaltered from their default settings.

540

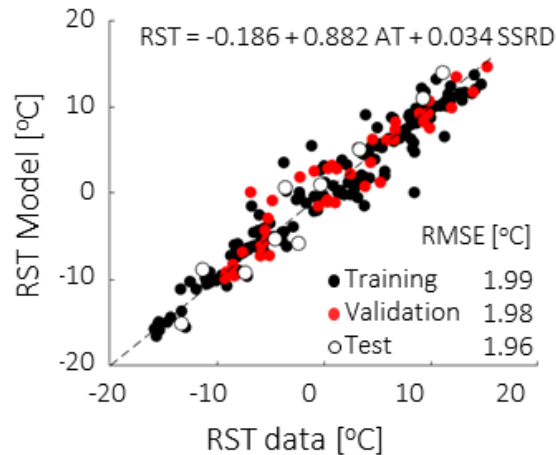


Figure 5. GST models summary. On top, examples Summary of model fit for the dataset RST model. The model is a (composite weather station data for 1850—2022) function of AT and b (ERA5 reanalysis for 1979—2022)SSRD. On bottom, table with training Data are aggregated at monthly time step. Training and validation performances for data are acquired to the four different GST modelsRST loggers. Test data are acquired by SIS2021-01.

545 To visualize the model performance, we plot the RMSE distribution between model and data is consistently below 0.1 across the borehole depth, as showed in figure Fig.6c. The maximum RMSE is measured at 1 m depth (4.02 °C), while it drops consistently below 0.20 °C for depth below 10 m, while above the depth of zero annual amplitude the model deviates up to 2 °C b.g.s.. When evaluating the RMSE over the entire measurement period, we observed values ranging from maximum of 0.70 °C at surface, to below 0.10 °C below 10 m b.g.s., to below 0.01 °C below 80 m b.g.s. (Fig.6c). To contextualize the model performance, we compare our results to Magnin et al. (2017), who use a similar transient modeling approach. It must be taken into account that a direct comparison is difficult as, in our case boreholes are on flat terrain, while Magnin et al. (2017) have data from boreholes drilled on vertical bedrock, arguably less influenced by lateral variability in ground characteristics and snow cover. Given this, Magnin et al. (2017) also observes large discrepancies between model and data from the rock surface down to 6 m depth. At 10 m depth, their model has performances varying from 0.70 °C to 0.01 °C from the measured data, depending on the borehole and time aggregation used. This indicates that our RMSE is comparable with their findings, further proving that this modeling approach is valuable for predicting rock temperatures where heat transfer is dominated by conduction. At shallower depths, advective heat transfer, due to water and air circulation in cracks, drives temperature patterns that can not be modelled by this approach. Although recent studies are developing numerical approaches to quantify these effects (Magnin et al., 2020), it is not currently possible to apply such methods beyond the site scale.

550

555

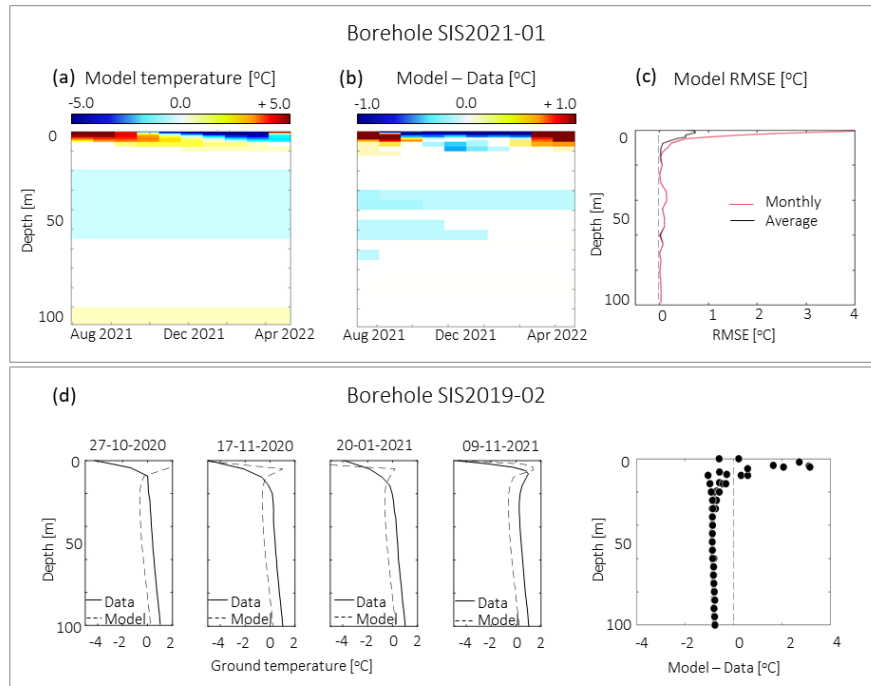


Figure 6. Summary of the heat transfer model calibration and testing with borehole data. All plots are issued by the model calibrated with the parameter values described in Sect. 4.3.3. Heat transfer model run for the observational period of SIS2021-01 (a). Difference between measured temperatures and model results at SIS2021-01 (b). RMSE between model and observations, aggregated at monthly time steps and over the entire observational period (c). Comparison between profile temperatures at SIS2019-01 and summary of model errors in function of borehole depth (d).

560 4.3.4 Model testing

When tested and compared to SIS2019-02 ($z = 55 \text{ m}$; $\text{PISR} = 690 \text{ kWhm}^{-2}$, $\text{SnowP} = 1$ Fig. 6d), the model produces similar results (Fig. ??b), indicating errors shows the same error pattern decreasing with depth observed for SIS2021-01, indicating discrepancies up to $2 \text{ }^\circ\text{C}$ above the depth of zero annual amplitude (20 m depth), while the errors are consistently smaller than $0.15 \text{ }^\circ\text{C}$ below this depth. Considering that all temperature profiles at this location were recorded in fall - early winter, it seems that the model over-estimates shallow rock temperatures during this period. These cold anomalies in the measured data could be due to advective heat transfer processes in the rock cracks, possibly enhanced by the flat terrain, e.g. cold rain infiltration.

4.4 Permafrost mapping

The permafrost map is represented by the MGT20, i.e. the average temperature at 20 m depth (below the depth Concerning the temperatures below the depth of zero annual amplitude) during the period 2012-2022 (Fig. 8a and b). Overall, the model

570 indicates that 81 km² (57% of the study area) has negative MGT20. Spatial distribution of permafrost is summarized in a polar plot (Fig. 8c), showing the relationship linking ground temperatures and the predictors aspect and elevation. At sea level, north facing slopes can reach negative MGT20 when snow free. Negative MGT20 can be found on south slopes starting at 200 m.a.s.l.. The colder MGT20 occurs on the north faces of the Nasaasaq peak (763 m.a.s.l.), reaching -4.0. the model shows a cold bias, with values 0.85 °C. Snow cover plays an important role, as snow covered areas can increase of 250 m the elevation of the

575 MGT20 0 C to 0.75 °C isotherm. This effect is prominent on mountain flanks characterized by sequences of ridges and chutes (Fig.8b), as the chutes are warmer than the ridges due to their predisposition to accumulate snow. C lower than the data. We believe this effect is due to the fact that this borehole is located in an area of recurrent snow drift accumulation, as explained in Sect. 4.1. In particular, our model does not take into account snow accumulation and it represents ground temperatures in an hypothetical snow-free location with the same AT and SSRD as in SIS2019-02. The difference between our model and

580 the borehole data suggests that recurrent snow cover has a warming effect on deep ground temperatures, which the analysis indicates to be of 0.80 °C. Considering this effect, summed to the model RMSE distribution described in the previous section, our model results can deviate -1.0°C to 0.2°C from the data below 10 m.b.g.s.. When snow cover exists, our model is colder than the actual deep rock temperatures, reason why this temperature interval is skewed towards the negative temperatures. This temperature range describes our uncertainty range when predicting rock permafrost conditions in areas where snow may or

585 may not accumulate, i.e. generic bedrock terrain. In the following analysis we will refer to this uncertainty range as *transition zone*. Similarly to the transition zone described for the ERT tomogram in Sect. 4.2, here our heat transfer model results are uncertain in discerning frozen form unfrozen ground conditions.

Summary of modelled ground temperature distribution in the study site. The parameters used to describe ground temperature here is the average ground temperature at 20 meters depth in the past ten years. On panel a, study site map colored by MGT20. On panel b, 3D view of the Nasaasaq range from East. On panel c, polar plot of the distribution of MGT20 based on slope aspect (0° is north) and elevation (outer radius is sea level, increasing to 800 masl at the center.

590

4.3.1 Comparison between 2D model and ERT profile

In Fig. 3e is presented. As additional model test, we present the 2D model simulation at the geophysical profile location . The model indicates, as of October 2020, the presence of negative temperatures below the depth of annual amplitude on the

595 Nattoralinguaq summit, suggesting the presence of permafrost . The south face is (Fig.7). According to the numerical model output, 55 % of the ERT transect area shows frozen ground conditions, while 2 % is expected to be in unfrozen conditions. 43 % of the transect is within the transition zone, i.e. the numerical model predicts a rock temperature within -1.0 °C and 0.2 °C and the model is uncertain in assigning either frozen or unfrozen conditions within this range. Similar values are provided by the ERT tomogram (48 % frozen, 37 % transition and 15% unfrozen). Overall, the model and the ERT tomogram have a 74

600 % agreement, although the model predicts generally colder conditions than the ERT tomogram. It is unclear whether it is our numerical model to overestimate permafrost extents, or conversely the ERT tomogram to underestimate permafrost extents.

In particular, the model shows the lower section of the south face of the mountain to be permafrost free, with ground temperatures above zero at 20-40 10-20 m depth. The north face on the other hand, reaches temperatures below Below the

summit and towards the south face side of the mountain, temperatures are in the range of 0.5 to -1 °C. By comparing the model results with ~~indicating a transition zone between frozen and unfrozen ground. This pattern of warm south face with transitioning conditions from frozen to unfrozen is in agreement with the ERT tomogram, although the latter method shows a larger unfrozen area. The numerical simulation predicts negative temperatures across the whole north face. This pattern is confirmed by the ERT tomogram, which shows frozen conditions on the upper part of the ERT data (Fig.3b), we can observe a qualitative agreement between the two datasets, as they both indicate the presence of sporadic permafrost on the summit. Both datasets indicate a mostly unfrozen south face, and a colder north face. However, the ERT data indicate a large unfrozen section at the extremity face, albeit being the unfrozen area expected to be smaller. As explained in Sect. 4.2, the lower section of the north face is characterized by the presence of a lithological fault affecting the ERT tomogram, and any comparison with the numerical simulation is meaningless here.~~

4.3.1 Permafrost evolution in future scenarios: RCP 2.6 and RCP 8.5

Future scenarios simulations are conducted both at the landscape scale (Fig.??c) and at SIS2021-01 location (Fig.??a and ??b). The simulations conducted at SIS2021-01 show that, regardless the scenario used, permafrost conditions will disappear by the end of the 21st century. For scenario RCP 2.6, the ground seems in phase transition by 2100, being at 0.05–0.1 °C between 50 and 70 meters depth. For scenario RCP 8.5 ground temperatures are consistently above 0.3 °C. In 2100, ground temperatures at 20-50 m depth are about 1 to 2.5 °C higher for Overall, the RCP 8.5 compared to RCP 2.6, indicating that, due to thermal inertia of the ground, surface heat is not yet fully propagated at depth by 2100 in this scenario. ~~two models show agreeing patterns of permafrost distribution, as they both indicate discontinuous permafrost across the mountain and a dominance of the SSRD in discerning between frozen and unfrozen conditions. We consider the 74% agreement between the two methods as satisfactory, as it is sufficient for us to confirm the main permafrost patterns at this location.~~

~~At the landscape level, any future scenario causes a significant reduction in the extents of frozen grounds by 2100 (Fig.??c)~~

625 4.4 Permafrost distribution and expected evolution

According to our RST model, during the period 2002-2022, 63% of the rock walls (i.e. 5.85 km²) have negative MRST and likely host permafrost, as summarized in the polar plot in Fig.8a. North facing rock walls can reach negative MRST already at sea level, while south facing rock walls are likely to host permafrost starting at 500 m.a.s.l.. The colder MRST occurs on the north faces of the Nasaasaq peak (763 m.a.s.l.), reaching -3.0 °C. For the RCP 2.6, in 2090-2100 is simulated a slight (Fig.8b), in 2080-2100 is simulated an increase in elevation of the MGT20 isotherm by about MRST 0 °C isotherm of 150 m. This causes a widespread loss of permafrost grounds, from 81-9% loss of rock wall permafrost extents, from 5.85 km² (57% of the study area) to 53 to 5.31 km² (37%). For the scenario RCP 8.5 the impact on permafrost is more severe severe (Fig.8c), as, in the period 2080-2100, as permanently frozen ground disappears from most of the study area, except for the highest summits and covering 4 north faces of the highest summits covering 0.08 km² (3 less than 1% of the rock walls in the study area) in the period 2090-2100. The MGT20 0 °C isotherm elevation increases above the 700 m.a. s.l. on south faces, while on north faces, we observe a retreat of the MGT20 0

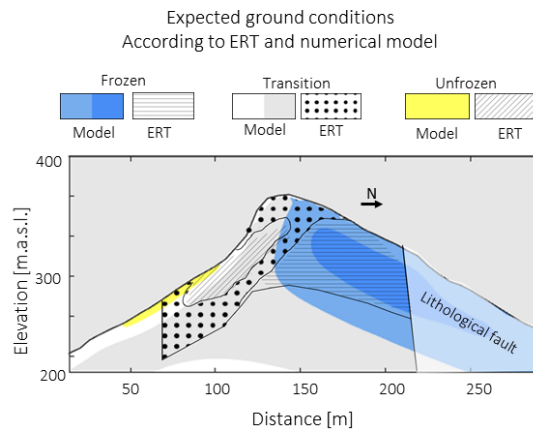


Figure 7. Comparison between the 2D heat transfer model run at the ERT transect location and the ERT data. Ground is described with respect to its conditions, varying from frozen and unfrozen. Transitional conditions indicate the uncertainty range of the two methodologies in discerning frozen from unfrozen ground conditions. The colors indicate ground conditions as described by the heat transfer model, while patterned areas indicate ground conditions as described by the ERT tomogram.

While the MRST maps show the impacts of future climate change on the surface, numerical simulations quantify the ground temperatures below the surface. The simulations conducted at SIS2021-01 show that, regardless the scenario used, permafrost conditions will disappear by the end of the 21st century (Fig.9a). For scenario RCP 2.6, the lowest ground temperature is modeled at 60 m.b.g.s., reaching 0.07 °C isotherm up to 500 m.a. s.l. (Fig.9b). For scenario RCP 8.5 ground temperatures are consistently above 0.22 °C (Fig.9b). In 2100, ground temperatures at 20-50 m depth are about 1 to 1.5 °C higher for the RCP 8.5 compared to RCP 2.6, indicating that, due to thermal inertia of the ground, surface heat is not yet fully propagated at depth by 2100 in this scenario.

A similar result is obtained when evaluating the expected ground temperature evolution in complex terrain by the 2D models model (Fig.??10). For Nattoralinnguaq, the optimistic scenario (the ERT location (Fig. 10a), the model forced with the scenario RCP 2.6) suggests an increase of ground temperatures of about 1 the temperatures of the permafrost body of 0.7 °C, causing permafrost retreat on the north face up to 200 m. a.s.l. minimum ground temperatures to be within our model transition zone. This indicates that, at this location, permafrost is expected to exist at temperatures close to thawing point and only underneath extensive snow free areas. Scenario RCP 8.5 delineates a situation where permafrost is relict, i.e. transitioning conditions still exist, but constrained below the reach of seasonal frost (Magnin et al., 2017), at approximately 100 m depth on the 15 m depth below the surface of the north face. The model produce This indicates that all permafrost on the mountain is relict, as defined by (Magnin et al., 2017), and survives only thanks to the thermal inertia of the ground. The model produces similar results for Nasaasaq (Fig. 10b), as for scenario RCP 2.6 we observe permafrost retreat to 300 m.a.s.l. on the north face and to 500 m.a.s.l.

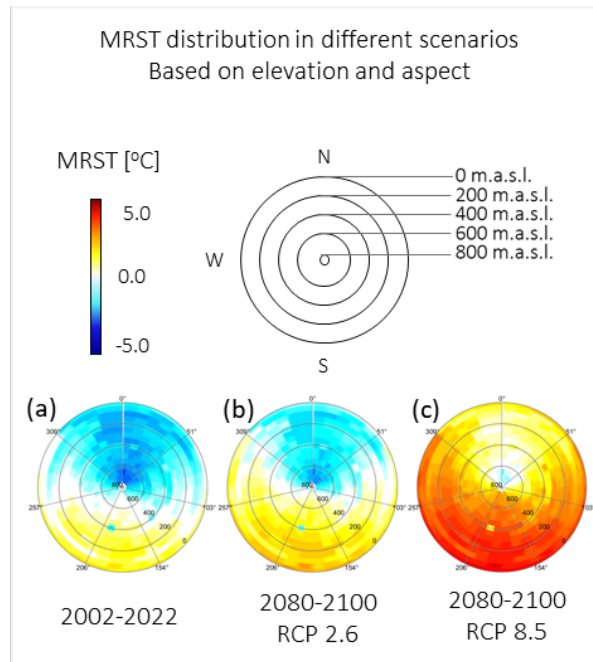


Figure 8. Summary of rock wall MRST distribution at different times and scenarios. The summary are presented as polar plots, where the color-coded MRST is presented as a function of aspect and elevation. RST distribution is averaged over the periods 2002-2022 (a) and 2080-2010 for scenarios RCP 2.6 (b) and RCP 8.5 (c).

on the a point that the frozen body is below the reach of the seasonal frost on the whole south face. Scenario RCP 8.5 indicates
 655 that all permafrost on the mountain is relict, except for the summit's north face.

Summary of future scenarios from 1D models. Ground temperature evolution at SIS2021-01 (a). Comparison of mean ground temperature profiles (2090-2100) between optimistic and pessimistic scenarios (b). Landscape distribution of MGT20 as polar plots (elevation as radius, angle as slope aspect—0° points north) in 2022 and the two scenarios (c).

Modelled evolution of ground temperatures on Nattoralinnguaq (left column) and Nasaasaq (right column). The images are
 660 computed using the 2D model of ground temperature evolution.

5 Discussion

4.1 Model uncertainties and evaluation

Our modeling strategy is based on linking GST measurements to climate data downscaled with a topographical approach. Correlating GST with aspect and elevation only, as proxies of solar radiation and air temperature, disregards other processes
 665 such as near surface air advection and longwave radiation. Although our method also involves other weather parameters for the period 1979-2022, the basic assumption of linear relation between GST and topographical settings still holds. To better

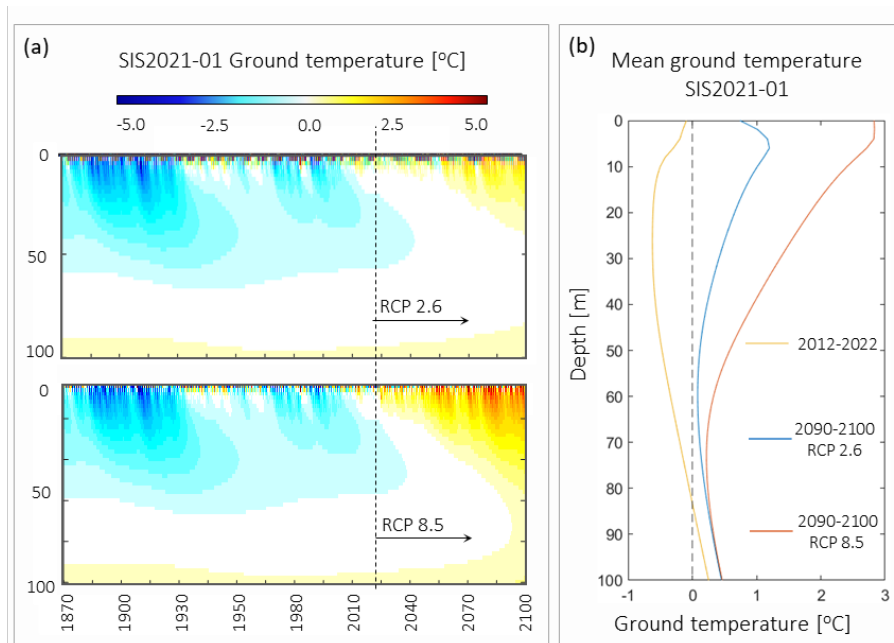


Figure 9. Summary of modeled evolution of temperatures at SIS2021-01. Temperature evolution over the period 1870-2100 depending on the different scenarios (a). Visualisation of temperature profiles as function of borehole depth for different periods and scenarios (b).

contextualize our results, we can compare our model to Schmidt et al. (2021) which represents the state of the art of numerical modeling of the physical processes affecting rockwall temperature in the arctic. Their approach is based on the SEB module of CryoGrid-3 modified to account for vertical terrain, including vertical moisture transport affected by latent heat flux and skyview factor adapted to steep terrain. By comparing model runs and field data, Schmidt et al. (2021) obtained $R^2 = 0.97$ and $RMSE = 1.2\text{ }^\circ\text{C}$ on monthly GST data, which is comparable to our model performance on the validation dataset c ($R^2 = 0.99$ and $RMSE = 1.6\text{ }^\circ\text{C}$). Although this comparison is encouraging, we suggest that the time period covered by our data is still too short (only one year) to fully understand the predictive performance of our modeling approach for GST-

A more reliable assessment of the model performance is given by comparing the results of the heat transfer module to the borehole and geophysical data. Although our model seems to provide good results (mean error of $0.14\text{ }^\circ\text{C}$ from The common thread shown by these results is that the study area is going to experience a reduction in the extents of permafrost in rock walls by 2100, regardless the scenario considered. This due to the fact that permafrost in the area is discontinuous and already close to thawing point as of 2022. Even in scenario RCP 2.6, which causes a relatively mild increase in ATs compared to the current conditions, the numerical simulations forecast an increase of deep ground temperatures near 0 to 100 m depth, Fig.??), we shall compare our results to Magnin et al. (2017), who use a similar modeling approach, to better understand this performance. It must be taken into account that a direct comparison is difficult as, in our case boreholes are on flat terrain, which are influenced by lateral variations in snow accumulation and surface characteristics. Magnin et al. (2017) on the other hand have data from

boreholes on drilled vertical bedrock, arguably less influenced by lateral variability in ground characteristics and snow cover. Given this, Magnin et al. (2017) reaches an average difference between modelled and measured temperatures of 0.01 °C at 10 m depth, indicating a better performance than our model. Since most of the disagreement between borehole data and our model occur in the upper 10 m, we believe that this performance difference is likely imputable to our climatic database. While Magnin et al. (2017) had near-in situ long term weather station data, our data come mostly from global reanalysis, and seem to be not precise enough to explain short term variability in ground temperatures. Overall, we suggest that our model is not suitable for describing short term variability of ground temperatures above the depth of zero annual amplitude.

On the other hand, our model is more reliable when describing ground temperatures below the depth of zero annual amplitude. Here, the model has a maximum error of 0.15 °C when compared to SIS2019-02, which is used only as validation dataset. SIS2019-02 has also different snow conditions than SIS2021-01, suggesting that the offset method is suitable to model long term effect of recurrent snow cover induced by topographical patterns. It has to be highlighted that the SnowP map failed to properly identify snow conditions for SIS2021-01 location, suggesting that the performance of this method in flat terrain is not yet satisfactory. However, the general agreement between model and geophysical data indicates that the model is suitable for describing permafrost extents in complex terrain. Most of the disagreement between model and geophysical data is due to the electrical conductivity anomaly on the north face of the geophysical profile. This anomaly occurs near a large lithological fault, visible in the field. Overall, the observations indicate that ground characteristics at this location are not isotropic and a direct comparison between model and geophysics is not meaningful. All this considered, the results indicate that the modeling approach is suitable for evaluating of ground temperatures below the depth of zero annual amplitude in complex terrain. This is achieved with using forcing data available at the Greenland scale, making an significant step towards a comprehensive assessment of mountain permafrost in the region.

4.1 Local permafrost distribution compared to other regions

We can use our results to compare the distribution of bedrock permafrost in the Sisimiut area to other mountain ranges, as presented in Fig.???. Ground surface temperatures in rockwalls seems comparable to conditions described in Northern Norway (69–71° N), where permafrost can be found at sea level on north facing slopes (Magnin et al., 2019). In Sisimiut, the solar radiation creates an average offset of 2.4 °C from north to south facing slopes, causing a rise of about 400 m of elevation in the permafrost mid elevations (200 - 400 m.a.s.l.). This corresponds to the disappearance of permafrost in most low elevation south facing slopes. Scenario RCP 8.5 is expected to have a critical impact on the rock wall permafrost patterns in the area. While permafrost bodies may keep on existing below ground surface even at 200 m.a.s.l. (Fig.10a), less than 1% of the rock walls are expected to have a MRST below 0 °C isotherm between this two aspects. This offset is known to be dependent on latitude, varying from 8 °C in the European Alps (45-46° N, Magnin et al. (2015a)) to 1.5 °C in Northern Norway (69-71° N, Magnin et al. (2019)). In coastal climates, previous studies suggested that steep bedrock permafrost could be influenced by other factors than pure solar radiation, as cloudiness and icing, creating an abnormally low offset in New Zealand (Allen et al., 2009). In this context, the north-south offset we measure in the Sisimiut area is consistent with the latitudinal trend obtainable by previous studies, suggesting that, despite the fact that the Sisimiut mountain area is coastal, pure

solar radiation is dominant on landscape-scale permafrost characteristics, after elevation-dependent air temperature variations.

720 Temperature offset between north and south facing rockwalls at different latitudes, retrieved from Magnin et al. (2015a)¹,
Allen et al. (2009)^{2, 2.3}, Magnin et al. (2019)⁴ and the present study⁵.

4.1 Future evolution of bedrock permafrost in the area and implications

725 Our model suggests that as of 2020 the deep ground temperatures are in disequilibrium with the current climate. This is highlighted by the fact that, even in scenario RCP 2.6, which causes a relatively mild increase in air temperatures and MGT20, the permanently frozen bedrock area will decrease by about 35% by 2090-2100. This corresponds to the disappearance of permafrost in most low elevation south facing slopes and plateaus, as well as an increase of by the end of the century, indicating that most rock wall permafrost in the active layer thickness for most of north facing slopes at low elevation. This situation becomes more critical with scenario RCP-area will become relict. Considering the strong temperature gradients between surface and deep rock temperatures (See RCP 8.5, where only 5% of permafrost ground existent in 2022 will outlast the 21st century. As highlighted by the 2D simulations, this does not involve a dramatic reduction of the deep frozen bodies, as they
730 will persist in form of relict permafrost well after the end of the 21st century. These results are comparable to the French Alps where on Fig.9b), it is arguable that even a stabilisation of the climate after 2100, the area will still experience a progressive decrease of rock wall permafrost extents.

735 These patterns of rock wall permafrost degradation are comparable to the expected evolution of rock wall permafrost at 3400 - 4000 m.a.s.l. in the French Alps described by Magnin et al. (2017). At their location, mountain permafrost is expected to re-
treat only on the highest summits of the Mont Blanc massif, while relict permafrozen bedrock only relict permafrost can persist at lower elevations (Magnin et al., 2017). These findings imply that in the near future permafrost degradation will affect most of the rockwalls rock walls in the Sisimiut area, creating the preliminary conditions for a possible increase in rockfall activity of both small and large magnitude (Krautblatter et al., 2013) as observed in the Mont Blanc massif (Ravel and Deline, 2011)

740 5 Conclusions

This study presents a first quantification of bedrock permafrost on mountain terrain in Sisimiut. In this study, we investigate present rock wall permafrost conditions and their expected evolution across the 21st century in the Sisimiut area, West Greenland, using a heat transfer module forced by simplified. Albeit localized in a small area, we have for the first time an assessment of rock wall permafrost conditions within the country. To describe rock wall permafrost here, we combine different data
745 sources, including RST data, borehole temperatures, a ERT tomogram and regionally-available weather data. The modeling approach produces results that are consistent with available data from deep boreholes and geophysical investigations. Based on our results, permafrozen bedrock-Rock temperatures are simulated using a combination of empirical and numerical models, applied both to 1D and 2D geometries. The main outcomes are the following:

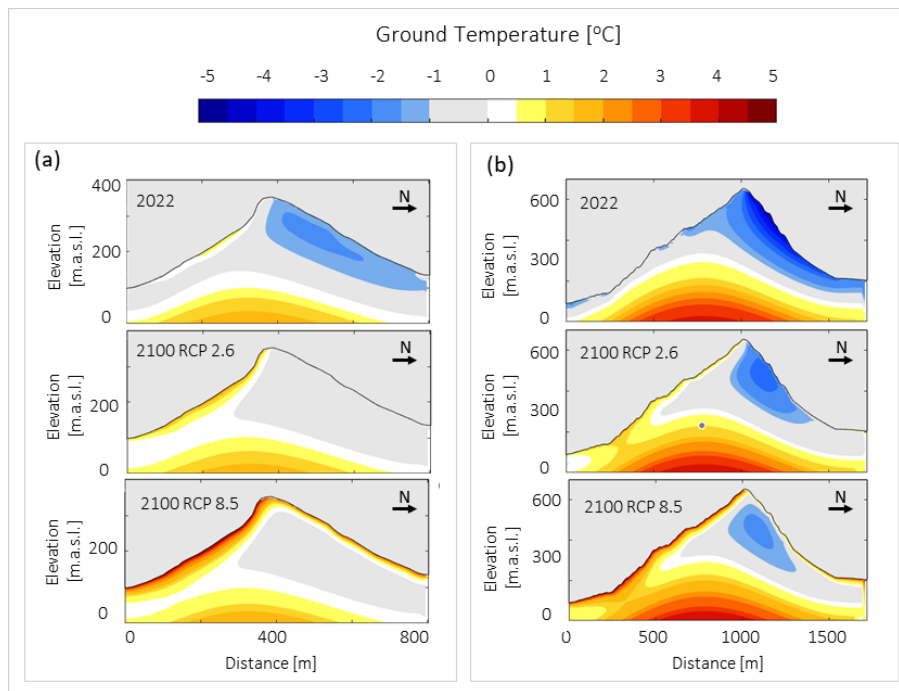


Figure 10. Summary of 2D simulations for future scenarios, 2D models are run until 2100 for RCP 2.6 and RCP 8.5 at the ERT location (a) and Nasaasaaq summit (b).

- 750 – The modeling results consistently replicate the patterns described by the available data. The modeling uncertainties are of a similar order of magnitude to those observed in previous studies that employed identical methodologies in different geographic locations. This modeling approach is therefore suited to describe permafrost patterns in the study area.
- 755 – The data show widespread evidence of discontinuous permafrost in the area. Permafrost can be found in rock walls and bedrock already in shaded locations at sea level on north-facing /snow-free slopes, while on south-facing slopes the lower margins are at about . South facing rock walls are observed to be permafrost free up to 400 m.a.s.l.. This indicates that, considering the local topography, most of the mountain terrain hosts temperate permafrost. Forcing our model with future climatic projections shows different degrees of permafrost degradation depending on the scenario considered. For scenario Measured permafrost temperatures are close to thawing point.
- 760 – Considering the optimistic scenario (scenario RCP 2.6), the model predicts a 9 % reduction of the extents of rock wall permafrost by the end of the 21st century. This will interest mostly the south faces, which will become permafrost-free at all elevations in the area. In this scenario, north faces may still host permafrost down to sea level.
- Considering the pessimistic scenario (scenario RCP 8.5, i.e. with no mitigation on carbon emissions, our), the model predicts a reduction of 95% of the active permafrost area at 99% reduction of the extents of rock wall permafrost by the

end of the century, meaning that permanently frozen ground will persist only as relict condition below 10-20 m depth, i.e. below the reach of 21 st century. Permafrost will survive only in relict bodies at the core of summits below 600 m.a.s.l. MRSTs are expected to be below 0 °C on north facing rock walls above 600 m.a.s.l.

765

- The current and future state of rock wall permafrost conditions in our study area closely resembles those described in the elevation range of 3300 to 4000 m.a.s.l. of the Mont-Blanc massif. Consequently, we hypothesize that this ongoing permafrost degradation forms the seasonal frost. This condition suggests a future strong disequilibrium between ground temperatures and climatic forcing, creating the basis for more frequent rockfall activity. An increase in rock fall and rock slide activity, as observed in Mont-Blanc area.

770

Although the correlation between permafrost degradation and rockfall activity is accepted within the scientific community (Raveland and Deline, 2011; Patton et al., 2019), the process chain linking the two phenomena is very complex. Therefore, future efforts in the area should focus on investigating Our modeling approach provides a good first assessment for rock wall permafrost zonation. Additional investigations of slope stability characteristics, and their relation to permafrost distribution and degradation . Once (and if) problematic slopes are identified, site specific models could aid in the further refinement of the proposed modeling approach. For potentially endangered slopes this could be achieved by integrating high resolution snow distribution (Haberhorn et al., 2016) and crack networks (Magnin et al., 2020) will provide, providing a more detailed understanding of slope thermodynamics, overcoming the main uncertainties of our model. Further efforts should also apply at larger scale, in order to characterize mountain permafrost in the whole region. In this sense, our modeling approach based on weather parameters readily available for the whole region, downscalable with a simple topographical approach, provides a good first assessment for mountain permafrost zonation. Moreover, future research activities should aim at the application of the proposed modeling approach for investigations at larger scales.

775

780

Author contributions. MM designed the study, conducted fieldwork and modeling. PAD conducted geophysical fieldwork and data processing. ST participated in geophysical fieldwork. SRN organised deep boreholes drillings. AR advised on geophysical data processing. TIN supervised the study, field logistics and data interpretation. All authors contributed to the manuscript.

785

Competing interests. No competing interests are present

Acknowledgements. This study is part of project TEMPRA and Siku Aajitsoq, funded by the Greenland Research Council. The study is also part of the Nunataryuk project, which is funded under the European Union's Horizon 2020 Research and Innovation Programme under Grant Agreement 773421. The deep boreholes were established as part of the Greenland Integrated Observing System (GIOS) funded by the Danish National Fund for Research Infrastructure (NUFI) under the Ministry for higher Education and Science. This work was realised in cooperation with EDYTEM and Styx4D. We acknowledge Jessy Lossel for his work on the rock samples.

790

References

- (Springer Series in Statistics) Emanuel Parzen, Kunio Tanabe, Genshiro Kitagawa (auth.), Emanuel Parzen, Kunio Tanabe, Genshiro Kitagawa (eds.)-Selected Papers of Hirotugu Akaike-Springer-Verlag New.pdf.
- 795 Allen, S. K., Gruber, S., and Owens, I. F.: Exploring Steep Bedrock Permafrost and its Relationship with Recent Slope Failures in the Southern Alps of New Zealand, 356, 345–356, <https://doi.org/DOI: 10.1002/ppp.658>, 2009.
- Bentsen, M., Bethke, I., Debernard, J. B., Iversen, T., Kirkevåg, A., Seland, Ø., Drange, H., Roelandt, C., Seierstad, I. A., Hoose, C., and Kristjánsson, J. E.: The Norwegian Earth System Model, NorESM1-M – Part 1: Description and basic evaluation of the physical climate, *Geoscientific Model Development*, 6, 687–720, <https://doi.org/10.5194/gmd-6-687-2013>, 2013.
- 800 Biskaborn, B. K., Smith, S. L., Noetzi, J., Matthes, H., Vieira, G., Streletskiy, D. A., Schoeneich, P., Romanovsky, V. E., Lewkowicz, A. G., Abramov, A., Allard, M., Boike, J., Cable, W. L., Christiansen, H. H., Delaloye, R., Diekmann, B., Drozdov, D., Etzelmüller, B., Grosse, G., Guglielmin, M., Ingeman-Nielsen, T., Isaksen, K., Ishikawa, M., Johansson, M., Johannsson, H., Joo, A., Kaverin, D., Kholodov, A., Konstantinov, P., Kröger, T., Lambiel, C., Lanckman, J. P., Luo, D., Malkova, G., Meiklejohn, I., Moskalenko, N., Oliva, M., Phillips, M., Ramos, M., Sannel, A. B. K., Sergeev, D., Seybold, C., Skryabin, P., Vasiliev, A., Wu, Q., Yoshikawa, K., Zheleznyak, M., and Lantuit, H.: Permafrost is warming at a global scale, *Nature Communications*, 10, 1–11, <https://doi.org/10.1038/s41467-018-08240-4>, 2019.
- 805 Boeckli, L., Brenning, A., Gruber, S., and Noetzi, J.: Permafrost distribution in the European Alps: calculation and evaluation of an index map and summary statistics, *The Cryosphere*, 6, 807–820, <https://doi.org/10.5194/tc-6-807-2012>, 2012.
- Brown, R. J. E.: The distribution of permafrost and its relation to air temperature in Canada and the U.S.S.R., *Arctic*, 13, 163–177, <https://doi.org/10.14430/arctic3697>, 1960.
- 810 Cappelen, J. and Jensen, D.: Climatological Standard Normals 1991-2020 - Greenland, Tech. rep., DMI - Danish Meteorological Institute, <https://www.dmi.dk/publikationer/>, 2021.
- Cappelen, J., Vinther, B. M., Kern-Hansen, C., Laursen, E. V., and Jørgensen, P. V.: Greenland-DMI Historical Climate Data Collection 1784-2020, Tech. Rep. May, www.dmi.dk<https://www.dmi.dk/publikationer/www.dmi.dk>, 2021.
- Colgan, W., Rajaram, H., Abdalati, W., McCutchan, C., Mottram, R., Moussavi, M. S., and Grisby, S.: Glacier crevasses: Observations, models, and mass balance implications, *Reviews of Geophysics*, 54, 119–161, <https://doi.org/doi:10.1002/2015RG000504>, 2016.
- 815 COMSOL Inc.: COMSOL Multiphysics, Heat Transfer Module User’s Guide, version 5.4, <https://doc.comsol.com/5.4/doc/com.comsol.help.heat/HeatTransferModuleUsersGuide.pdf>, 2015.
- Conrad, O., Bechtel, B., Bock, M., Dietrich, H., Fischer, E., Gerlitz, L., Wehberg, J., Wichmann, V., and Böhner, J.: System for Automated Geoscientific Analyses (SAGA) v. 2.1.4, *Geoscientific Model Development*, 8, 1991–2007, <https://doi.org/10.5194/gmd-8-1991-2015>, 2015.
- 820 Coperey, A., Revil, A., and Stutz, B.: Electrical Conductivity Versus Temperature in Freezing Conditions: A Field Experiment Using a Basket Geothermal Heat Exchanger, *Geophysical Research Letters*, 46, 14 531–14 538, <https://doi.org/10.1029/2019GL084962>, 2019.
- Czekirda, J., Westermann, S., and Etzelmüller, B.: Transient Modelling of Permafrost Distribution in Iceland, 7, 1–23, <https://doi.org/10.3389/feart.2019.00130>, 2019.
- 825 Czekirda, J., Etzelmüller, B., Westermann, S., Isaksen, K., and Magnin, F.: Post-Little Ice Age rock wall permafrost evolution in Norway, *The Cryosphere*, pp. 2725–2754, 2023.

- Daanen, R. P., Ingeman-Nielsen, T., Marchenko, S. S., Romanovsky, V. E., Foged, N., Stendel, M., Christensen, J. H., and Hornbech Svendsen, K.: Permafrost degradation risk zone assessment using simulation models, *Cryosphere*, 5, 1043–1056, <https://doi.org/10.5194/tc-5-1043-2011>, 2011.
- 830 Dahlin, T. and Zhou, B.: A numerical comparison of 2D resistivity imaging with 10 electrode arrays, *Geophysical Prospecting*, 52, 379–398, <https://doi.org/10.1111/j.1365-2478.2004.00423.x>, 2004.
- Delhasse, A., Kittel, C., Amory, C., Hofer, S., As, D. V., Fausto, R. S., and Fettweis, X.: Brief communication : Evaluation of the near-surface climate in ERA5 over the Greenland Ice Sheet, 5, 957–965, 2020.
- Duvillard, P., Ravel, L., Schoeneich, P., Deline, P., Marcer, M., and Magnin, F.: Cold Regions Science and Technology Qualitative risk
835 assessment and strategies for infrastructure on permafrost in the French Alps, 2021.
- Duvillard, P. A., Ravel, L., Marcer, M., and Schoeneich, P.: Recent evolution of damage to infrastructure on permafrost in the French Alps, *Regional Environmental Change*, 19, 1281–1293, <https://doi.org/10.1007/s10113-019-01465-z>, 2019.
- Duvillard, P.-A., Magnin, F., Revil, A., Legay, A., Ravel, L., Abdulsamad, F., and Coperey, A.: Temperature distribution in a permafrost-affected rock ridge from conductivity and induced polarization tomography, *Geophysical Journal International*, pp. 1207–
840 1221, <https://doi.org/10.1093/gji/ggaa597>, 2020.
- Etzelmüller, B.: Recent advances in mountain permafrost research, *Permafrost and Periglacial Processes*, 24, 99–107, <https://doi.org/10.1002/ppp.1772>, 2013.
- Etzelmüller, B., Czokir, J., Magnin, F., Duvillard, P. A., Ravel, L., Malet, E., Aspaas, A., Kristensen, L., Skrede, I., Majala, G. D., Jacobs, B., Leinauer, J., Hauck, C., Hilbich, C., Böhme, M., Hermanns, R., Eriksen, H. O., Lauknes, T. R., Krautblatter, M., and Westermann, S.:
845 Permafrost in monitored unstable rock slopes in Norway-New insights from temperature and surface velocity measurements, geophysical surveying, and ground temperature modelling, *Earth Surface Dynamics*, 10, 97–129, <https://doi.org/10.5194/esurf-10-97-2022>, 2022.
- Fettweis, X., Mabilille, G., Erpicum, M., Nicolay, S., and van den Broeke, M.: The 1958-2009 Greenland ice sheet surface melt and the mid-tropospheric atmospheric circulation, *Climate Dynamics*, 36, 139–159, <https://doi.org/10.1007/s00382-010-0772-8>, 2011.
- Fiddes, J. and Gruber, S.: TopoSUB: A tool for efficient large area numerical modelling in complex topography at sub-grid scales, *Geoscientific Model Development*, 5, 1245–1257, <https://doi.org/10.5194/gmd-5-1245-2012>, 2012.
- 850 Fiddes, J. and Gruber, S.: TopoSCALE v.1.0: Downscaling gridded climate data in complex terrain, *Geoscientific Model Development*, 7, 387–405, <https://doi.org/10.5194/gmd-7-387-2014>, 2014.
- Frauenfelder, R., Isaksen, K., Lato, M. J., and Noetzli, J.: Ground thermal and geomechanical conditions in a permafrost-affected high-latitude rock avalanche site (Polvartinden, northern Norway), *Cryosphere*, 12, 1531–1550, <https://doi.org/10.5194/tc-12-1531-2018>, 2018.
- 855 Gallach, X., Carcaillet, J., Ravel, L., Deline, P., Ogier, C., Rossi, M., Malet, E., and Garcia-Sellés, D.: Climatic and structural controls on Late-glacial and Holocene rockfall occurrence in high-elevated rock walls of the Mont Blanc massif (Western Alps), *Earth Surface Processes and Landforms*, 45, 3071–3091, <https://doi.org/10.1002/esp.4952>, 2020.
- GAPHAZ: Assessment of Glacier and Permafrost Hazards in Mountain Regions - Technical Guidance Document, Prepared by Allen, S., Frey, H., Huggel, C. et al. Standing Group on Glacier and Permafrost Hazards in Mountains (GAPHAZ) of the International Association of Cryospheric Sciences (IACS) and the International Permafrost Association (IPA). Zurich, Switzerland, p. 72, 2017.
- 860 Gislås, K., Westermann, S., Schuler, T. V., Litherland, T., Isaksen, K., Boike, J., and Etzelmüller, B.: A statistical approach to represent small-scale variability of permafrost temperatures due to snow cover, *Cryosphere*, 8, 2063–2074, <https://doi.org/10.5194/tc-8-2063-2014>, 2014.

- 865 Gislén, K., Eitzelmlüller, B., Lussana, C., Hjort, J., Sannel, A. B. K., Isaksen, K., Westermann, S., Kuhry, P., Christiansen, H. H., Framp-
ton, A., and Åkerman, J.: Permafrost Map for Norway, Sweden and Finland, *Permafrost and Periglacial Processes*, 28, 359–378,
<https://doi.org/10.1002/ppp.1922>, 2017.
- Gruber, S.: Derivation and analysis of a high-resolution estimate of global permafrost zonation, *Cryosphere*, 6, 221–233,
<https://doi.org/10.5194/tc-6-221-2012>, 2012.
- 870 Gruber, S., Hoelzle, M., and Haeblerli, W.: Rock-wall temperatures in the Alps: Modelling their topographic distribution and regional differ-
ences, *Permafrost and Periglacial Processes*, 15, 299–307, <https://doi.org/10.1002/ppp.501>, 2004.
- Gubler, S., Fiddes, J., Keller, M., and Gruber, S.: Scale-dependent measurement and analysis of ground surface temperature variability in
alpine terrain, *The Cryosphere*, 5, 431–443, <https://doi.org/10.5194/tc-5-431-2011>, 2011.
- Guerin, A., Ravel, L., Matasci, B., Jaboyedoff, M., and Deline, P.: The three-stage rock failure dynamics of the Drus (Mont Blanc massif,
France) since the June 2005 large event, *Scientific Reports*, 10, 1–21, <https://doi.org/10.1038/s41598-020-74162-1>, 2020.
- 875 Haberkorn, A., Wever, N., Hoelzle, M., Phillips, M., Kenner, R., Bavay, M., and Lehning, M.: Distributed snow and rock temperature
modelling in steep rock walls using Alpine3D, *The Cryosphere Discussions*, pp. 1–30, <https://doi.org/10.5194/tc-2016-73>, 2016.
- Hasler, A., Geertsema, M., Foord, V., Gruber, S., and Noetzli, J.: The influence of surface characteristics, topography and continentality on
mountain permafrost in British Columbia, *The Cryosphere*, 9, 1025–1038, <https://doi.org/10.5194/tc-9-1025-2015>, 2015.
- 880 Hersbach, H., Bell, B., Berrisford, P., Hirahara, S., Horányi, A., Muñoz-Sabater, J., Nicolas, J., Peubey, C., Radu, R., Schepers, D., Sim-
mons, A., Soci, C., Abdalla, S., Abellan, X., Balsamo, G., Bechtold, P., Biavati, G., Bidlot, J., Bonavita, M., De Chiara, G., Dahlgren,
P., Dee, D., Diamantakis, M., Dragani, R., Flemming, J., Forbes, R., Fuentes, M., Geer, A., Haimberger, L., Healy, S., Hogan, R. J.,
Hólm, E., Janisková, M., Keeley, S., Laloyaux, P., Lopez, P., Lupu, C., Radnoti, G., de Rosnay, P., Rozum, I., Vamborg, F., Vil-
laume, S., and Thépaut, J. N.: The ERA5 global reanalysis, *Quarterly Journal of the Royal Meteorological Society*, 146, 1999–2049,
<https://doi.org/10.1002/qj.3803>, 2020.
- 885 Hilbich, C., Hauck, C., Hoelzle, M., Scherler, M., Schudel, L., Völsch, I., Vonder Mühll, D., and Mäusbacher, R.: Monitoring mountain
permafrost evolution using electrical resistivity tomography: A 7-year study of seasonal, annual, and long-term variations at Schilthorn,
Swiss Alps, *Journal of Geophysical Research: Earth Surface*, 113, 1–12, <https://doi.org/10.1029/2007JF000799>, 2008.
- Hipp, T., Eitzelmlüller, B., and Westermann, S.: Permafrost in Alpine Rock Faces from Jotunheimen and Hurrungane, Southern Norway,
Permafrost and Periglacial Processes, 25, 1–13, <https://doi.org/10.1002/ppp.1799>, 2014.
- 890 Hofer, S., Lang, C., Amory, C., Kittel, C., Delhase, A., Tedstone, A., and Fettweis, X.: Greater Greenland Ice Sheet contribution to global
sea level rise in CMIP6, *Nature Communications*, 11, 1–11, <https://doi.org/10.1038/s41467-020-20011-8>, 2020.
- Isaksen, K., Lutz, J., Sørensen, A. M., Godøy, Ø., Ferrighi, L., Eastwood, S., and Aaboe, S.: Advances in operational permafrost monitoring
on Svalbard and in Norway, *Environmental Research Letters*, 17, <https://doi.org/10.1088/1748-9326/ac8e1c>, 2022.
- 895 Keuschnig, M., Krautblatter, M., Hartmeyer, I., Fuss, C., and Schrott, L.: Automated Electrical Resistivity Tomography Testing for
Early Warning in Unstable Permafrost Rock Walls Around Alpine Infrastructure, *Permafrost and Periglacial Processes*, 28, 158–171,
<https://doi.org/10.1002/ppp.1916>, 2017.
- Kneisel, C.: Assessment of subsurface lithology in mountain environments using 2D resistivity imaging, *Geomorphology*, 80, 32–44,
<https://doi.org/10.1016/j.geomorph.2005.09.012>, 2006.
- 900 Krautblatter, M. and Hauck, C.: Electrical resistivity tomography monitoring of permafrost in solid rock walls, *Journal of Geophysical
Research: Earth Surface*, 112, 1–14, <https://doi.org/10.1029/2006JF000546>, 2007.

- Krautblatter, M., Verleysdonk, S., Flores-Orozco, A., and Kemna, A.: Temperature-calibrated imaging of seasonal changes in permafrost rock walls by quantitative electrical resistivity tomography (Zugspitze, German/Austrian Alps), *Journal of Geophysical Research: Earth Surface*, 115, 1–15, <https://doi.org/10.1029/2008JF001209>, 2010.
- 905 Krautblatter, M., Funk, D., and Günzel, F. K.: Why permafrost rocks become unstable: A rock-ice-mechanical model in time and space, *Earth Surface Processes and Landforms*, 38, 876–887, <https://doi.org/10.1002/esp.3374>, 2013.
- Legay, A., Magnin, F., and Ravel, L.: Rock temperature prior to failure: Analysis of 209 rockfall events in the Mont Blanc massif (Western European Alps), *Permafrost and Periglacial Processes*, 32, 520–536, <https://doi.org/10.1002/ppp.2110>, 2021.
- Ljungdahl, B.: *Geologisk oversigt: Grønland*, 1967.
- Loke, M. H. and Barker, R. D.: Rapid least-squares inversion of apparent resistivity pseudosections by a quasi-Newton method, *Geophysical Prospecting*, 44, 131–152, <https://doi.org/10.1111/j.1365-2478.1996.tb00142.x>, 1996.
- 910 Magnin, F., Deline, P., Ravel, L., Noetzi, J., and Pogliotti, P.: Thermal characteristics of permafrost in the steep alpine rock walls of the Aiguille du Midi (Mont Blanc Massif, 3842 m a.s.l.), *Cryosphere*, 9, 109–121, <https://doi.org/10.5194/tc-9-109-2015>, 2015a.
- Magnin, F., Krautblatter, M., Deline, P., Ravel, L., Malet, E., and Bevington, A.: Determination of warm, sensitive permafrost areas in near-vertical rockwalls and evaluation of distributed models by electrical resistivity tomograph, *Journal of Geophysical Research: Earth Surface*, 120, 2452–2475, <https://doi.org/10.1002/2014JF003351>.Received, 2015b.
- 915 Magnin, F., Josnin, J. Y., Ravel, L., Pergaud, J., Pohl, B., and Deline, P.: Modelling rock wall permafrost degradation in the Mont Blanc massif from the LIA to the end of the 21st century, *Cryosphere*, 11, 1813–1834, <https://doi.org/10.5194/tc-11-1813-2017>, 2017a.
- Magnin, F., Westermann, S., Pogliotti, P., Ravel, L., Deline, P., and Malet, E.: Snow control on active layer thickness in steep alpine rock walls (Aiguille du Midi, 3842 m a.s.l., Mont Blanc massif), *Catena*, 149, 648–662, <https://doi.org/10.1016/j.catena.2016.06.006>, 2017b.
- 920 Magnin, F., Etzelmüller, B., Westermann, S., Isaksen, K., Hilger, P., and Hermanns, R. L.: Permafrost distribution in steep slopes in Norway: measurements, statistical modelling and geomorphological implication, *Earth Surface Dynamics Discussions*, pp. 1–35, <https://doi.org/10.5194/esurf-2018-90>, 2019.
- Magnin, F., Josnin, J., Magnin, F., Water, J. J., Permafrost, R., and Coupling, A.: *Water Flows in Rockwall Permafrost : a Numerical Approach Coupling Hydrological and Thermal Processes* To cite this version : HAL Id : hal-03024087 *Water Flows in Rockwall Permafrost : a Numerical Approach Coupling Hydrological*, 2020.
- 925 Marcer, M., Stentoft, P. A., Bjerre, E., Cimoli, E., Bjørk, A., Stenseng, L., and Machguth, H.: Three Decades of Volume Change of a Small Greenlandic Glacier Using Ground Penetrating Radar, Structure from Motion, and Aerial Photogrammetry, *Arctic, Antarctic, and Alpine Research*, 49, 411–425, <https://doi.org/10.1657/AAAR0016-049>, 2017.
- Marcer, M., Cicoira, A., Cusicanqui, D., Bodin, X., Echelard, T., Obregon, R., and Schoeneich, P.: Rock glaciers throughout the French Alps accelerated and destabilised since 1990 as air temperatures increased, *Communications Earth Environment*, pp. 1–12, <https://doi.org/10.1038/s43247-021-00150-6>, 2021.
- 930 Myhra, K. S., Westermann, S., and Etzelmüller, B.: Modelled Distribution and Temporal Evolution of Permafrost in Steep Rock Walls Along a Latitudinal Transect in Norway by CryoGrid 2D, 182, 172–182, <https://doi.org/10.1002/ppp.1884>, 2017.
- Noetzi, J. and Gruber, S.: Transient thermal effects in Alpine permafrost, *Cryosphere*, 3, 85–99, <https://doi.org/10.5194/tc-3-85-2009>, 2009.
- 935 Noetzi, J., Gruber, S., Kohl, T., Salzmann, N., and Haeberli, W.: Three-dimensional distribution and evolution of permafrost temperatures in idealized high-mountain topography, *Journal of Geophysical Research: Earth Surface*, 112, 1–14, <https://doi.org/10.1029/2006JF000545>, 2007.

- Obu, J., Westermann, S., Bartsch, A., Berdnikov, N., Christiansen, H. H., Dashtseren, A., Delaloye, R., Elberling, B., Etzelmüller, B., Kholodov, A., Khomutov, A., Kääb, A., Leibman, M. O., Lewkowicz, A. G., Panda, S. K., Romanovsky, V., Way, R. G., Westergaard-Nielsen, A., Wu, T., Yamkhin, J., and Zou, D.: Northern Hemisphere permafrost map based on TTOP modelling for 2000–2016 at 1 km scale, *Earth-Science Reviews*, 193, 299–316, <https://doi.org/10.1016/j.earscirev.2019.04.023>, 2019.
- 940
- Parr, C., Sturm, M., and Larsen, C.: *Snowdrift Landscape Patterns : An Arctic Investigation*, *Water Resources Research*, 56, <https://doi.org/10.1029/2020WR027823>, 2020.
- Patton, A. I., Rathburn, S. L., and Capps, D. M.: Landslide response to climate change in permafrost regions, *Geomorphology*, 340, 116–128, <https://doi.org/10.1016/j.geomorph.2019.04.029>, 2019.
- 945
- Pellet, C. and Noetzi, J.: *Swiss Permafrost Bulletin 2018/2019, Permos 2020 (Swiss Permafrost Monitoring Network)*, pp. 1–20, <https://doi.org/10.13093/permos-2019-01.Cover>, 2020.
- Porter, C.: *ArcticDEM, Version 3*, 2018.
- QGIS: QGIS Geographic Information System, QGIS.org. Last accessed September 2023, 2023.
- 950
- Rasmussen, L. H., Zhang, W., Hollesen, J., Cable, S., Christiansen, H. H., Jansson, P. E., and Elberling, B.: Modelling present and future permafrost thermal regimes in Northeast Greenland, *Cold Regions Science and Technology*, 146, 199–213, <https://doi.org/10.1016/j.coldregions.2017.10.011>, 2018.
- Ravanel, L. and Deline, P.: Climate influence on rockfalls in high-alpine steep rockwalls: The north side of the aiguilles de chamonix (mont blanc massif) since the end of the 'Little Ice Age', *Holocene*, 21, 357–365, <https://doi.org/10.1177/0959683610374887>, 2011.
- 955
- Rico, I., Magnin, F., López Moreno, J. I., Serrano, E., Alonso-González, E., Revuelto, J., Hughes-Allen, L., and Gómez-Lende, M.: First evidence of rock wall permafrost in the Pyrenees (Vignemale peak, 3,298 m a.s.l., 42°46'16''N/0°08'33''W), *Permafrost and Periglacial Processes*, pp. 673–680, <https://doi.org/10.1002/ppp.2130>, 2021.
- Scandroglio, R., Draebing, D., Offer, M., and Krautblatter, M.: 4D quantification of alpine permafrost degradation in steep rock walls using a laboratory-calibrated electrical resistivity tomography approach, *Near Surface Geophysics*, 19, 241–260, <https://doi.org/10.1002/nsg.12149>, 2021.
- 960
- Schmidt, J. U., Etzelmüller, B., Schuler, T. V., Magnin, F., Boike, J., Langer, M., and Westermann, S.: Surface temperatures and their influence on the permafrost thermal regime in high Arctic rock walls on Svalbard, *The Cryosphere*, 15, 1–29, <https://doi.org/10.5194/tc-2020-340>, 2021.
- Stocker-Mittaz, C., Hoelzle, M., and Haeberli, W.: Modelling alpine permafrost distribution based on energy-balance data: a first step, *Permafrost and Periglacial Processes*, 13, 271–282, <https://doi.org/10.1002/ppp.426>, 2002.
- 965
- Strzelecki, M. C., Jaskólski, M. W., and Strzelecki, M. C.: Arctic tsunamis threaten coastal landscapes and communities -Survey of Karrat Isfjord 2017 tsunami effects in Nuugaatsiaq, western Greenland, *Natural Hazards and Earth System Sciences*, 20, 2521–2534, <https://doi.org/10.5194/nhess-20-2521-2020>, 2020.
- Svennevig, K.: Preliminary landslide mapping in Greenland, *GEUS Bulletin*, 43, 1–5, 2019.
- 970
- Svennevig, K., Hermanns, R. L., Keiding, M., Binder, D., Citterio, M., Dahl-Jensen, T., Mertl, S., Sørensen, E. V., and Voss, P. H.: A large frozen debris avalanche entraining warming permafrost ground—the June 2021 Assapaat landslide, West Greenland, *Landslides*, 19, 2549–2567, <https://doi.org/10.1007/s10346-022-01922-7>, 2022.
- Svennevig, K., Keiding, M., Korsgaard, N. J., Lucas, A., Owen, M., Poulsen, M. D., Priebe, J., Sørensen, E. V., and Morino, C.: Uncovering a 70-year-old permafrost degradation induced disaster in the Arctic, the 1952 Niiortuut landslide-tsunami in central West Greenland, *Science of the Total Environment*, 859, <https://doi.org/10.1016/j.scitotenv.2022.160110>, 2023.
- 975

- Walls, M., Hvidberg, M., Kleist, M., Knudsen, P., Mørch, P., Egede, P., Taylor, G., Phillips, N., Yamasaki, S., and Watanabe, T.: Hydrological instability and archaeological impact in Northwest Greenland: Sudden mass movement events signal new concerns for circumpolar archaeology, *Quaternary Science Reviews*, 248, 106 600, <https://doi.org/10.1016/j.quascirev.2020.106600>, 2020.
- 980 Walter, F., Amann, F., Kos, A., Kenner, R., Phillips, M., de Preux, A., Huss, M., Tognacca, C., Clinton, J., Diehl, T., and Bonanomi, Y.: Direct observations of a three million cubic meter rock-slope collapse with almost immediate initiation of ensuing debris flows, *Geomorphology*, 351, 106 933, <https://doi.org/10.1016/j.geomorph.2019.106933>, 2020.
- Westermann, S., Langer, M., Boike, J., Heikenfeld, M., Peter, M., Eitzelmüller, B., and Krinner, G.: Simulating the thermal regime and thaw processes of ice-rich permafrost ground with the land-surface model CryoGrid 3, *Geoscientific Model Development*, 9, 523–546, <https://doi.org/10.5194/gmd-9-523-2016>, 2016.
- 985 Wood, J.: Geomorphometry in LandSerf, *Developments in Soil Science*, 33, 333–349, [https://doi.org/10.1016/S0166-2481\(08\)00014-7](https://doi.org/10.1016/S0166-2481(08)00014-7), 2009.